

Part One
Metal Oxide Nanomaterials

1

The Biomimetic Synthesis of Metal Oxide Nanomaterials

Leila F. Deravi, Joshua D. Swartz and David W. Wright

1.1

Introduction

Traditionally, synthetic approaches for the production of functional metal oxide materials have involved high-temperature reaction environments with energy-intensive techniques such as laser ablation, ion implantation, chemical vapor deposition (CVD), photolithography or thermal decomposition [1]. The incorporation of these techniques has provided a rapid prototyping technique, essential for the commercial development of current minimum feature-sized semiconducting integrated circuits. However, the production of these devices has been achieved at a high price, with the primary challenges currently faced by high-throughput fabrication laboratories including the high cost of laborers and instruments, high-temperature reaction conditions, and a surplus in generated waste [1]. In fact, the cost of fabrication facilities are estimated to reach an outstanding US\$100 billion per facility by the year 2020, as the demand for smaller, lighter and faster materials continues to grow [1]. But, more importantly, manufacturers are progressing in this manner at the expense of the environment, as they accumulate hazardous chemical wastes [2]. For decades, research teams in the semiconductor industry have been seeking alternative methods to passivate not only the rate of waste production but also the cost of spending.

The most accessible resource for the synthesis of functional materials under ambient conditions is found in biology. From highly ordered nanostructures to genetically controlled reactive surfaces, systems in biology perpetually demonstrate their ability to find effective solutions to multifaceted, real-world problems using a rigorous process of natural selection [3–7]. The versatility of biology's incredible portfolio encourages researchers to develop modified syntheses derived from Nature. Hence, their findings have been successfully organized into the field of biomimetics, or bioinspired research, which encompasses alternative approaches towards developing nanomaterials with technological applications [8]. Based primarily on the designs, mechanisms and processes found in Nature, biomimetics

encompasses the field of structural biology while interfacing engineering, materials science, physics and chemistry [4, 8].

Biomimetics infers the manipulating and mimicking of natural architectures and processes of biologically produced minerals (biominerals) to direct the synthesis of non-natural materials. For instance, the architecture of one of the most abundant biological species on the planet—the virus—has recently been manipulated to serve as containers for the synthesis of a variety of functional molecular cargoes [9, 10]. In particular, the positively charged interior of the cowpea chlorotic mottle virus (CCMV) has been used as a container for the nucleation of spatially confined metal oxide nanomaterials [10]. On a larger and more complex scale, versatile strategies for substrate modification have been developed directly, through inspiration from the surface-mediated mineralization of biological organisms [3]. The eggshell matrix proteins from the Chinese soft-shelled turtle (composed primarily of aragonite, CaCO_3) were isolated, and revealed properties that are necessary for embryonic survival [3]. It was suggested that the matrix proteins contained pelovaterin peptides as their major unit that self-assembled into micelles, altering the interfacial energy of the eggshell [11]. Applications of such controlled mineralization could be applied to the successful construction of functional two-dimensional (2-D) reactive surfaces, with reduced nonspecific adsorption [12–15].

Bioinspired research is based on identifying and emulating the principles of biomineralization in natural systems, instead of copying them directly. In fact, most strategies incorporated by natural systems are not directly applicable to engineered materials, so the need for alternative synthetic routes are required for the incorporation of non-natural elements, such as barium, nickel, copper or aluminum, with functional nanoscale properties [1, 8]. From a materials perspective, highly intact biological structures such as diatoms, bacteria, proteins or butterfly wings provide an excellent source of inspiration for their synthesis. In this chapter we have included the details of a wide variety of mediated nanomaterial syntheses, their response to variable parameters, and their ability to retain a functionalized, controlled stability over time.

1.2 Metal Oxides in Nature

To date, as many as 60 biominerals have been identified as being necessary for the correct function of organisms, and more than 60% of these are reported to be coordinated to either hydroxyl moieties or water molecules, enabling the rapid release of ions in solution [7]. Metal oxides, in particular, provide a fundamental stepping-stone for the development of functional nanomaterials. In an oxidative environment, such as the atmosphere of the Earth, oxides are the lowest free energy states for most metals in the Periodic Table and demonstrate applications ranging from semiconductors to insulators [16]. As insulators, SiO_2 and Al_2O_3 are the two most commonly used supports for catalysis, as they are nonreducible

oxides [16]. Semiconductors, such as ZnO and SnO₂, have high electrical resistivities that provide alternative templates for gas sensors [16].

Surprisingly, the properties associated with metal oxides in technology are not so far removed from what is observed in natural systems. Through precisely tuned processes, Nature is able to synthesize a variety of metal oxide nanomaterials under ambient conditions; the magnetic navigation device found in magnetotactic bacteria (MTB) is one such example [17]. Here, magnetite (Fe₃O₄) nanocrystals are aligned with the Earth's geomagnetic field and contained within specific organelles known as magnetosomes [17]. Fresh water salmon, for example, utilizes these magnetic nanoparticles in the nasal cavities of their forehead as a biomagnetic compass during migration [18].

1.2.1

Components of Biomineralization

Nature dictates the basic structure and function of metal oxides in biology by a set of genetically controlled rules. In order to utilize these principles as inspiration for a variety of non-natural biomaterial syntheses, we must first understand their purpose. For example, organic ligands in the form of an amino acid side chain, lipids or carbohydrates—all of which are found in biological systems—direct the assembly of highly structured metal oxide nanomaterials [19]. Free metal ions act as Lewis acids in the hydrolysis of a precursor before it completely binds to the donor ligand (Lewis base) [20]. In addition, most of these metals in Nature follow similar trends, as laid out by the hard–soft acid–base (HSAB) theory [20]. The charge associated with the Lewis acid metal facilitates an energetically favorable nucleophilic attack on the carbonyl of the ligand. Because of the effective charge of the metal–ligand coordination, there are two alternative ways that this attack can occur. ‘Soft metals’ (Pt²⁺, Au²⁺, Cu²⁺, Cd²⁺) that are large and polarizable with low oxidation states bind with ‘soft ligands’ (carbonyls, CN⁻, RS⁻) in order to balance their charge [20]. However, ‘hard metals’ (first row transition metals) are smaller and less polarizable, and are balanced by accepting lone pair electrons associated with ‘hard ligands’, such as H₂O, amines, phosphates or alcohols [20]. The ligand donor type can affect the redox potential of the coordinated metal, its stereochemistry, and its subsequent reactivity within a biological system.

With that in mind, there are several examples in Nature where ligands are used to create metal oxide structures. In order to identify the components that adhere specifically to metal surfaces, various research groups have developed methods for screening libraries of up to 10⁷ protein or peptide sequences that are responsible for inducing specific metal oxide mineralization [21, 22]. Once the sequence is selected, optimal peptide- or non-peptide-based mimics can be synthesized and subsequently applied to a wide range of nanomaterial syntheses. Among the techniques developed to isolate specific metal-bound peptides or proteins, phage display (PD) and cell surface display (CSD) are the most widely used [19, 21]. Combinatorial PD is used to specify the selectivity of the peptide–substrate interaction. In this method, a phage is created on an ensemble of bacterial particles, each

displaying different combinations of amino acids that are fused to the surface protein of the metal particle [23]. Peptides bound specifically to the crystal surface are then eluted from the surface, amplified using the polymerase chain reaction (PCR), and re-reacted up to five separate times [19]. After the fourth and fifth cycles, the resultant phage is sequenced, and the peptide responsible for binding to the surface of the crystal is identified [19].

An alternative approach to identifying surface ligands is that of CSD. Here, the process involves an analytical approach for the quantification of binding constants and dissociation rates *in situ* of up to 10^4 protein molecules per cell [24]. CSD permits the isolation of proteins that display ligand-binding, catalytic or electrochemical properties. Protein libraries on a specific cell surface can be labeled with a soluble ligand and quantitatively screened for reactivity by using flow cytometry [24]. Although, the identification of biomolecules specific for a metal is crucial in developing a particular biomimetic synthesis, it must be understood that peptides and proteins, alone, are not responsible for metal oxide formation in biology. In fact, the properties of these biomolecules *in situ* are a direct result of their reaction environment [25].

1.2.2

Biom mineralization Optimization

From the supramolecular to the cellular level, assemblies of lipids, glycoproteins or nucleotides in Nature are necessary determinants, defining specific reaction sites along organelles, membranes or cell walls [20]. Understanding the basic theory, process and components behind the biom mineralization of metal oxides is the first step in developing functional biomimetic materials. As noted before, the strategies and precursors incorporated by natural systems cannot be directly applied to engineered materials. For this reason, alternative routes are necessary to build and optimize the properties specific to metal oxide nanomaterials. The specific reaction conditions (length of reaction time, pH) are often tailored, depending on the desired structure and reactivity of the material; however, a typical approach to biomimetic synthesis often requires a developed precursor, in the form of a metal salt, suspended or dissolved in an aqueous medium, and coordinated to a structure-directing agent. Both, natural (peptides, starches, proteins) and synthetic (dendrimers, block copolymers) polymers can be used as structure-directing agents for inducing the biom mineralization of metal oxides [6]. They assemble in an ionic solution to direct the size, shape and mean distribution of the resultant product. Recent investigations have even incorporated surface-modified macromolecular templates in the form of a polystyrene latex bead, to direct the control and morphology of metal oxides (Figure 1.1).

Previously, diblock copolymers of ethylene oxide (EO), methacrylic (MAA) and double hydrophilic graft copolymers (PMAA or poly(vinyl sulfonate) backbones) were used separately without the latex beads to synthesize ZnO nanoparticles. It was demonstrated that the electrostatic charge associated with copolymers of vinyl-sulfonate exhibit a more active range of control over the resultant structure than

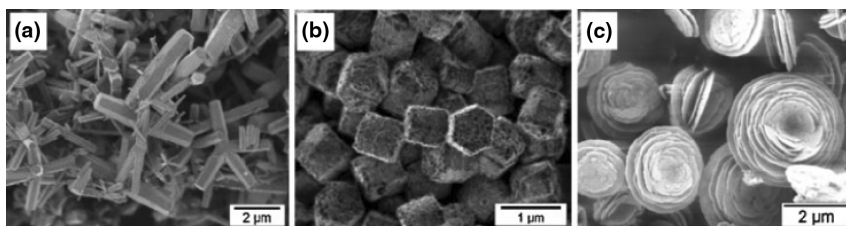


Figure 1.1 Zinc oxide materials synthesized (a) in the absence of latex beads, (b) in the presence latex beads functionalized with 9 g l^{-1} of poly(styrene-acrylic acid), and (c) latex beads (removed by calcinations at 600°C) functionalized with 3 g l^{-1} poly(styrene-maleic acid). Latex beads can be easily synthesized using mini-emulsion polymerization, and their functional surfaces tuned for specific ZnO properties. Reproduced with permission from Ref. [6]; © 2007, Wiley-VCH Verlag GmbH & Co. KGaA.

others did at the same fraction [6]. The activity of vinyl-sulfonate was optimized by anchoring it onto a hierarchical, supramolecular network of latex beads, thus demonstrating an alternative approach to controlling the synthesis of ZnO. As shown in Figure 1.1, ZnO was precipitated in the presence of the beads, yielding hybrid polymer–inorganic materials with various morphologies [6].

Control over the shape of a nanoparticle can affect not only the particle in isolation but also its interaction with other particles. However, the impact on the specific size of the material can determine the magnetic, electronic and chemical properties of nanoparticles [26, 27]. Such size-dependency has been observed in $\gamma\text{-Fe}_2\text{O}_3$ nanoparticles, with 55 nm particles exhibiting ferromagnetic behavior while their 12 nm counterparts produced superparamagnetic behavior, but with no hysteresis [18]. The chemical reactivity of the smaller nanoparticle will be enhanced due to its larger surface area per unit mass. Moreover, the decreased particle size will also decrease the overall magnetic anisotropy of the particle, thus inducing the change to superparamagnetic [28]. Novel methods of creating metal oxide nanoparticles of a defined size are necessary for achieving not only desired magnetic properties, but also electronic and chemical properties.

1.3 Biomimetic Synthesis of Metal Oxide Nanomaterials

In its most basic form, a material synthesized on the nanoscale infers a smaller, more reactive particle. In order to exercise control over the design and presentation of a particle in this size regime, several research groups have developed alternative approaches to synthesizing nanostructured materials under ambient conditions [29]. The well-defined, structural organization witnessed in biologically derived minerals such as these has inspired low-temperature syntheses that are favorable because they minimize the onset of particle degradation, which is often a factor in high-temperature reaction processes [30]. Generally, a biomineral can be induced, controlled or mediated by its reaction environment [3]. Induced syntheses

are most common in single-celled organisms, such as fungi or bacteria, and typically occur within a charged, open environment. The mineralized product remains dynamic and typically does not have a specific function within the system [7, 18, 20].

Biologically controlled, or constrained, reactions yield minerals with a minimal size distribution that are localized to a confined area, defined by a cell wall, lipid bilayer or vesicle [7]. This mineralized product has functional properties that are dependent on its origin of synthesis (extra-, inter- or intracellularly) [3, 20]. On the other hand, biologically mediated mineralization is often genetically controlled by the organism within unconstrained, open environments, while incorporating peptides, proteins, nucleic acids or polymers as templates during synthesis [3]. For instance, the proteins in diatoms, radiolarian and sponges produce SiO_2 that serves as their exoskeleton in the ocean, while biopolymers associated with echinoderms and nacreous layers mediate the production of single calcite crystals that serve as their protective coating [29, 31]. The valuable properties associated with constrained or unconstrained metal oxide synthesis in specific biological systems has inspired the development of functionalized nanomaterials, and these will be discussed here.

1.4 Constrained Biomineralization

Synthetic control over the physical and chemical properties of a nanoparticle can be tuned according to its biological micro- or nano-environment. Some of the most notable platforms that are currently being used for the controlled synthesis of metal oxides include the apoprotein ferritin, viral capsids or bacterial cages; however, recently adapted biotemplates, such as self-assemble peptide nanorings or porous butterfly wings, have been used as unique platforms and have yielded interesting structures. These molecular architectures offer constrained environments that yield a small distribution of nanoparticle size under ambient conditions, and will be discussed as viable alternatives for the synthesis of functional nanomaterials.

1.4.1 Bacterial Synthesis of Metal Oxide Nanomaterials

At least one-third of the elements in the Periodic Table have experienced changes in valence states induced by microbial activity. While some metals (iron, calcium, potassium) serve as an essential source for nutrients in bacterial systems, others are introduced as contaminants (lead, nickel, cobalt, cadmium) [2]. This cohabitation with such heavy-metal pollutants has forced organisms among marine bacteria to develop a high metal tolerance, which in turn makes them an interesting source for templating the constrained synthesis of metal/metal oxide nanoparticles.

Magnetic metal oxides nanoparticles have aroused particular interest because their properties can be tuned according to their size and shape. Exchange coupling at the interface of ferri/ferromagnetic and antiferromagnetic phases, as seen in nanoscale materials, can be applied as high-density magnetic storage devices or components for enhanced sensor development. Current wet-chemistry approaches, demonstrating control over the magnetic exchange bias of a nanoparticle, require expensive organometallic precursors and high-temperature reaction conditions. On the other hand, biologically produced microbes reduce metal ions in aqueous media to form stable suspensions of nanoparticles coated with biomolecules (proteins, peptides). This coating not only activates the modified properties of the nanoparticle, but also prevents particle agglomeration, thus stimulating the growth of discrete nanoparticles within a solution.

1.4.2

Synthesis of Protein-Functionalized Ferromagnetic Co_3O_4 Nanocrystals

A marine bacterium culture (obtained from the Arabian seacoast) has been used as the host system for the constrained synthesis of cobalt oxide (Co_3O_4) [2]. In this synthesis, the precursor, cobalt acetate (Co^{2+}) was incubated with the bacterium in an aqueous solution, and the as-synthesized particles displayed average diameters of 6 nm. After mild calcination (200 °C for 2 h), the particles grew larger (50 nm), inferring that its protein-passivating layer had degraded, causing particle aggregation. Of the 15 strains isolated from the bacterium culture, only one gave a visible indication of the formation of nanoparticles. Phylogenetic sequencing revealed that this oligonucleotide strand could potentially be the source of hydrolysis and reduction of the precursor salt [2].

At room temperature, bulk Co_3O_4 has been synthesized with a cubic spinel, antiferromagnetic phase. On the nanoscale, however, Co_3O_4 adapts an overall ferromagnetic type behavior because the uncompensated spins at the nanoparticle surface becomes a large fraction of the total number of spins. The as-synthesized nanoparticles were characterized using X-ray diffraction (XRD) and identified as crystalline. After heating above 930 °C (a reducing environment), the composite material was transformed into the CoO phase, which suggested that, at room temperature, Co_3O_4 is the thermodynamically preferable state [2]. Despite there being a dominant presence of Co^{3+} ions, X-ray photoelectron spectroscopy (XPS) identified trace amounts of Co^{2+} within the Co_3O_4 composite. Among the 24 Co-ions in the Co_3O_4 unit cell, it was predicted that eight Co^{2+} ions were located in the tetrahedral sites and 16 Co^{3+} ions in the octahedral sites. This mixed-valence state within the unit cell was understood to be the cause of the nanoparticle's overall magnetic moment (Figure 1.2).

The mechanism behind the oxidation of the cobalt precursor and subsequent Co_3O_4 precipitation within the bacterium host (Co^{2+} to Co^{3+}) was examined. A nonspecific intake of toxic Co ions within the host forced a spontaneous reaction that was balanced by the homeostasis of the system through developed resistance mechanisms. Through the basics of biology, it was predicted that Co^{2+} enters and

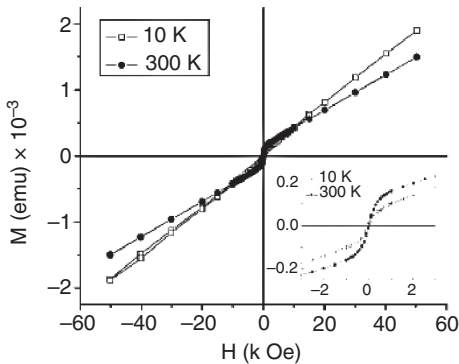


Figure 1.2 Magnetization versus magnetic field measurements of Co_3O_4 shows a nonlinear reversible behavior once calcined at 10 and 300 K. The plot did not show saturation until the highest applied field (50 kOe), which is a result of nonzero net

moment and ferromagnetic-type behavior of nanoparticles with Co^{3+} at octahedral sites. The inset shows an exaggerated view of the region of hysteresis. Reprinted with permission from Ref. [2]; © 2006, American Chemical Society.

exits the cell through an efflux pump, during which process Co^{2+} was either filtered through a cation diffusion facilitator (CDF) or was exported by resistance nodulation cell division (RND) proteins. Either way, the bacterial capsule was understood to bind and concentrate the metal ions along its walls, forming a cooperative, self-organized colony to resist induced external stress. This possible interbacterial communication involved in oxidizing precursor ions has exposed valuable properties associated with constrained synthesis, and can be used to control the synthesis of a number of additional metal oxides.

1.4.3

Room-Temperature Synthesis of Barium Titanate

As a source for nonvolatile memory, microelectromechanical device, or thin-film capacitor, barium titanate (BT) is an important electroceramic material with ferroelectric properties [32]. Most reported room-temperature syntheses have produced a cubic, paraelectric-phased BT; however, sub-10-nm, tetragonal and ferroelectric phases are desirable for successful implementation within miniaturized devices. For this reason, a purely biological approach was used to synthesize BT nanoparticles with constrained sizes using the plant pathogenic fungus *Fusarium oxysporum* as the host system. Aqueous solutions of barium acetate ($(\text{CH}_3\text{COO})_2\text{Ba}$) and potassium hexafluorotitanate (K_2TiF_6) were reacted with *F. oxysporum* [32]. The fungal proteins were responsible for the hydrolysis and confinement of these precursor materials, inducing BT nanoparticles. The free Ba^{2+} and acetate ions released from barium acetate were understood to coordinate to the free TiF_6^{2-} ions, using the extracellular proteins in the fungus. In order to approximate the percentage of biomaterial attached to the particle, the sample was

heated to 400 °C, after which thermogravimetric analysis (TGA) determined that there was up to 50% weight loss from the starting material. Both, transmission electron microscopy (TEM) and XPS were used to identify the BT nanoparticles (which had a size distribution of 4 ± 1 nm), while selected-area electron diffraction (SAED) was used to confirm that the particles were in the tetragonal phase.

Both, differential scanning calorimetry (DSC) and superparamagnetism (SPM) were used to probe the ferroelectricity of the as-synthesized nanoparticles and at various degrees of calcination. When SPM was used to investigate the polarizability of the nanoparticles in the ferroelectric phase, the peak broadening in the maxima of the temperature-dependent dielectric response and the DSC maximum at ferroelectric transition suggested that the as-synthesized particles behaved as a ‘ferroelectric relaxer’ material. Results indicated that BT nanoparticles were successfully written and read on a substrate in response to an applied external electric field. This confirmed that reactivity, coupled with the biologically constrained synthesis of sub-10 nm BT particles, is thought to revolutionize microelectronics industries. Hence, this method represents a nonvolatile and economically feasible alternative to current solid-state techniques for the production of highly controlled functional nanomaterials.

1.4.4

Biomimetic Synthesis of Magnetite

Iron oxides are technologically relevant metal oxides because, like cobalt oxide, they possess multivalent oxidation states that can be tuned specifically for an application, such as a catalytic template in sensor development or a substrate for drug delivery. Magnetite (Fe_3O_4), which is naturally found in the magnetosomes of MTB or other iron-reducing bacteria, is a well recognized example of controlled biomineralization [17, 18]. Once crystallized intracellularly, magnetite nanoparticles align with the Earth’s magnetic field to serve as a navigational compass for a number of aquatic animals [18]. Salmon, for example, utilize the magnetite located in their head for magnetic navigation that can last up to three years over tens of thousands of kilometers [18].

The morphology of magnetite varies according to the different bacterial strains associated with the lipid membrane of the magnetosome (Figure 1.3), as the membrane defines the biochemical composition of the subsequent metal oxide. A number of successful biomimetic approaches aimed at modifying the biological synthesis of magnetite have been developed, incorporating constrained biological environments. These mimics can be tuned by either chemical or genetic modification to yield interesting properties that are technological significant.

1.4.4.1 **Biomimetic Synthesis of Iron Oxide**

The magnetic properties of iron oxides, specifically magnetite, are of particular interest to materials scientists because they are associated with potential applications, ranging from magnetic storage devices to magnetic resonance imaging (MRI) contrast agents [17]. Unfortunately, the biosynthesis of magnetite can often

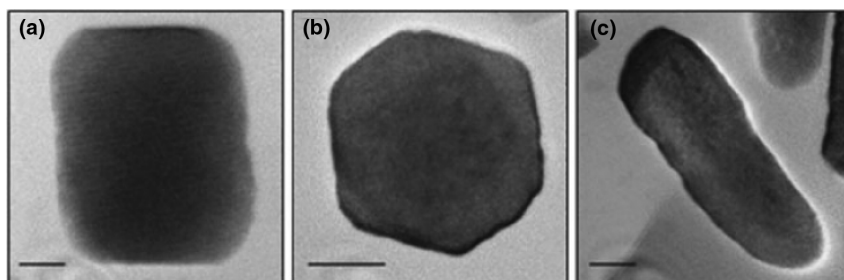


Figure 1.3 Transmission electron microscopy images (scale bar = 20 nm) of magnetosomes from various bacterial strains. (a) Pseudo-hexagonal prism; (b) Cubo-octahedral crystal; (c) Tooth-shaped. Reproduced with permission from Ref. [17]; © 2007, Wiley-VCH Verlag GmbH & Co. KGaA.

be slow (one week) under unfavorable anaerobic conditions; however, varying the reaction conditions (such as length of reaction time, pH) or starting materials has revealed several interesting properties associated with the nanoparticles. The chemical synthesis of various phases of iron oxide using alfalfa bioreduction (*Medicago sativa*) was completed and examined under low-magnification microscopy and elemental analysis (30 micrographs per sample) [33].

Varying the reaction conditions has produced different species of iron oxides while maintaining nanometer control (>10 nm) over the distribution of nanoparticles. The smallest nanoparticles were synthesized at pH 10 (3.6 ± 1.6 nm), and this led to a generation of magnetite clusters which coexisted with wuestite-like clusters. A preference for magnetite formation was exhibited at pH values of 7 and 10. A multimodal distribution of average sizes of nanoparticles was evidenced at pH 3 (6.2 ± 3.4 nm), whereas at pH 5 the mean particle size was increased to 7.2 ± 2.5 nm. At pH 7 and 10, the particle sizes were 4.1 ± 1.9 and 3.5 ± 1.6 nm, respectively (Figure 1.4). The chemical potential required to reduce the metal oxide system has been affected by the variation in pH, as indicated by the distribution in the size and phase of iron oxide composites.

Both, high-resolution TEM images and fast Fourier transformed (FFT) spectra were used to determine the structure of the resultant iron oxide. At pH 3, both rounded and irregular-shaped nanoparticles had planar spacings corresponding to the wuestite-like iron oxide ($\text{Fe}_{0.902}\text{O}$ cubic phase) at different zone axes. At pH 5, the nanoparticles had a slightly different morphology that showed two domains in one particle; the larger domain was subsequently analyzed and shown to have characteristic angles matching magnetite-like iron oxide (Fe_3O_4). A second particle studied had a more homogeneous structure, which corresponded to a wuestite-like particle. At pH 7 there was evidence of both wuestite and magnetite clusters that were similarly oriented within the same region. However, at pH 10 several particles within the same region were noted to have cubic-like arrays with a hexagonal

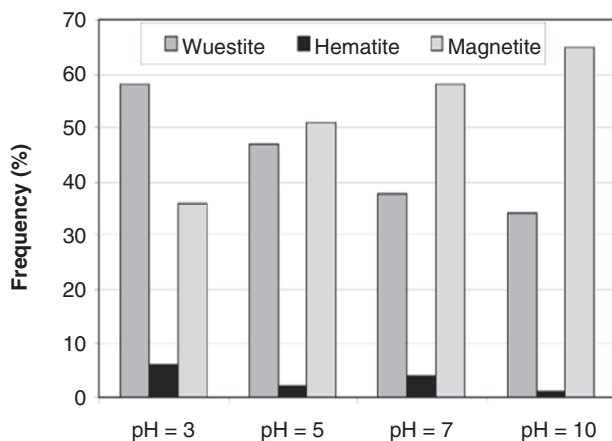
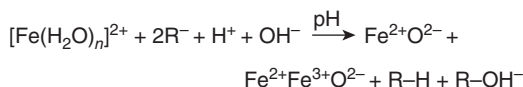
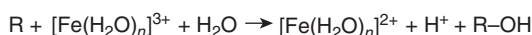
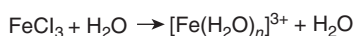


Figure 1.4 Distribution of structures for variable pH samples. Reprinted with permission from Ref. [33]; © 2007, American Chemical Society.



Scheme 1.1 Reprinted with permission from Ref. [33]; © 2007 American Chemical Society.

profile and a hexagonal internal contrast that matched the wuestite and magnetite structures.

The cations within the magnetite unit cell (fcc close-packed lattice of oxygen anions) were responsible for the induction of zig-zag or square shapes. In each unit cell, the lattice array was either octahedral (eight Fe^{2+} in each cation site) or a homogeneously distributed among tetragonal and octahedral (16 Fe^{3+}) packed sites. Hematite models have a signature hexagonal distribution with rectangular arrays, associated with Fe^{3+} cation packing, and are predominately seen in syntheses conducted at pH 3 (6% compared to negligible amounts found in the four other syntheses).

Powder-milled alfalfa (garlic acid, denoted as 'R' in the reactions in Scheme 1.1) was used to reduce the iron in the Fe component in this synthesis. The variation in crystal morphologies was generated according to the amount of Fe^{2+} available for reaction in the final step, while the pH-dependent morphology of the metal nanoparticles exposed the preferential reduction of iron into Fe^{2+} during the bio-synthesis process.

1.4.5

Metal Oxide Synthesis within a Protein Cage—Ferritin

The defined architecture of the metalloprotein ferritin, a natural complex of iron oxide, is found in almost all domains of life and has been used as a constrained reaction vessel for the synthesis of a number of non-natural metal oxides [28, 34]. The protein ferritin consists of 24 subunits that self-assemble into a cage, consisting of a threefold hydrophilic channel coordinated to a fourfold hydrophobic channel [20, 28]. In biology, Fe(II) is introduced into the core of the apoprotein through its hydrophilic channels; where the ferrous ion is catalytically oxidized to a less-soluble ferric ion, Fe(III) [20]. The ferric ion then undergoes a series of hydrolytic polymerizations to form the insoluble ferric oxyhydroxide mineral (ferrihydrite), which is physically constrained by the size of the protein cage (12 nm outer diameter, 8 nm inner diameter) [35]. The enzyme ferrous oxidase is coordinated within the protein cage, the interior and exterior of which is electrostatically dissimilar, to produce spatially defined minerals.

1.4.5.1 Mineralization of Non-Natural Metal Oxides Using Ferritin

The photoinduced mineralization of iron, titanium and europium oxyhydroxide nanoparticles has been successfully achieved using the protein cage, ferritin [35]. This photochemical reduction closely resembles the Fe(III) to Fe(II) reduction of marine siderophores with a citrate background [35]. In this synthesis, a known concentration of metal ion was loaded into a 12 mM solution of citrate and ferritin, and illuminated with a xenon arc lamp (320–750 nm) for over 2 h. The citrate solution induced an electrostatic environment that was essential for discrete nanoparticle synthesis in the reaction, without which the bulk precipitation was illuminated. After a 2 h reaction time, the high oxidation state metal ions were photoreduced, whereas in the presence of air the lower state underwent reoxidation to the final, oxyhydroxide state. All products were characterized using dynamic light scattering (DLS) and found to have similar sizes (12 ± 1 nm). Samples stained with uranyl acetate were analyzed with TEM, while the intact protein cage was visible, forming an outer diameter around the metal oxide cores of 5.7 ± 1 nm.

1.4.5.2 Mixed Mineralization Using Ferritin

Oxidation of the iron core in ferritin was used and applied to the mixed mineralization reactions of cobalt and iron. It is understood that, if synthesized correctly, this composite material would have tailored magnetic properties, inducing the exchange coupling of ferro/anti-ferromagnetic properties; wherein, the exchange bias is self-manifested and defined by a unidirectional hysteresis loop. Control over the magnetic behavior of a nanoparticle could, potentially, lead to additional magnetic anisotropy effects for use as magnetic storage and recording devices. Klem and coworkers have demonstrated the constrained synthesis of $\text{Co}_x\text{Fe}_{3-x}\text{O}_4$ with an exchange bias by means of an enhanced magnetic response [28].

For this synthesis, a deaerated solution of iron $[(\text{NH}_4)_2\text{Fe}(\text{SO}_4) \cdot 6\text{H}_2\text{O}]$, cobalt $[\text{Co}(\text{NO}_3)_2 \cdot 6\text{H}_2\text{O}]$ and H_2O_2 was added to apoferritin in NaCl (pH 8.5, 65 °C, under

nitrogen), and the reaction allowed to continue until a homogeneous, dark brown solution was formed. Light-scattering measurements showed no increase in the average diameter of ferritin after metal encapsulation. TEM images showed the core sizes to be consistent with the inner diameter of the ferritin (6.8–7.4 nm diameter), while SAED indicated that with 33% Co doping, the d -spacings were consistent with the spinel phase of Co_3O_4 and the inverse spinel magnetite phase of Fe_3O_4 . When using a rapid (5 min) synthetic method, Co is likely incorporated into the rapidly forming Fe_3O_4 lattice, which has enhanced the blocking temperature, inducing a loss in exchange bias. Under slow synthesis conditions (30 min), however, it was suggested that Fe_3O_4 formation would precede the nucleation and growth of Co_3O_4 on the basis of standard reduction potentials (Fe^{3+} and Co^{3+} are 0.771 and 1.808, respectively). The magnetic properties of the complex nanoparticle can be tuned according to its applications, depending on the mode of synthesis.

1.4.6

Viral Templates for Metal Oxide Synthesis

Conceptually, viruses and the metalloprotein ferritin are similar in that they are both assembled protein cages that serve as a host system for mineralized guest materials [9, 10]. The function of ferritin is to store and transport iron oxyhydroxide, while that of virus capsids is to store and transport organic polymers or nucleic acids [9, 20, 36]. Viruses are composed of repeating subunits which assemble into highly symmetric architectures that provide templates for nanoengineering biominerals. As molecular containers, viruses have three important interfaces: (i) the exterior; (ii) the interior; and (iii) the interfacial region of the protein subunits (Figure 1.5) [9]. Because the exterior surface of the viral capsid

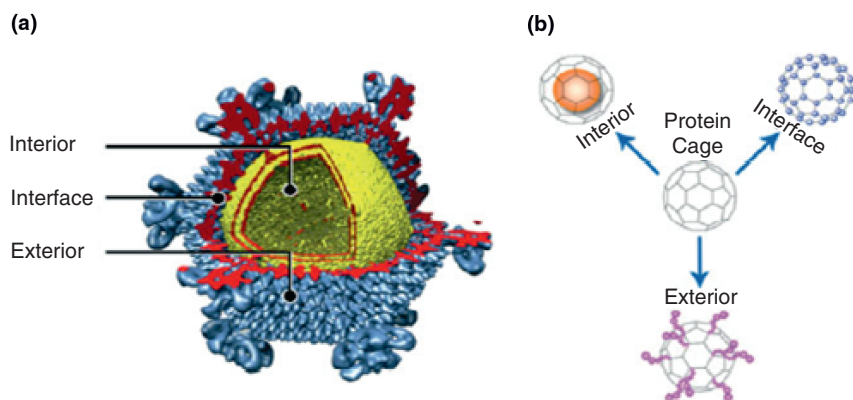


Figure 1.5 (a) Cryoelectron microscopy reconstruction of icosahedral symmetry of *Sulfobolus turreted virus*; (b) Three interfaces within a protein cage available for modification. Reproduced with permission from Ref. [36]; © 2007, Wiley-VCH Verlag GmbH & Co. KGaA.

is highly symmetric, every functional group is spatially defined over the entire cage; thus, the reactive sites can be genetically engineered for multivalent ligand presentation [36].

The capsid interior has been used to direct nanoparticle synthesis; for instance, the basic, positively charged interior of the cowpea chlorotic mottle virus (CCMV) has been utilized for the mineralization of a range of polyoxometalate species [9, 10]. In this synthesis, empty virions were incubated with precursor ions (WO_4^{2-} , VO_3^- , MoO_4^{2-}) at neutral pH, whereupon the virus exits in its open, or swollen, state will provide a pathway for ions to flow into and out of the cavity [10]. At pH 5.0, the capsid pores close to induce oligomerization, yielding large polyoxometalate crystals. The mineralized particles are then isolated and purified by centrifugation on sucrose gradients, and their subsequent size distribution is documented using TEM.

The interface between the capsid interior and exterior is defined by a series of noncovalently bound peptides. Within the icosahedral formation of the CCMV are 60 pores, each 2 nm in diameter, that open and close to allow ions and molecules to enter the interior, thus serving as a method of communication between interior and exterior. Because the virus capsid is a metastable, dynamic structure, the manipulation of its composition could introduce major structural changes from its original icosahedral formation to a sheet-like or tubular morphology. However, modifying the virus exterior with small molecules or biological ligands could have potential applications ranging from surface display or cell targeting to drug delivery [9]. Controlling the ligands associated with the virus can also be used to identify specific peptide or protein communications, similar to the commonly practiced phage display methods [9]. Identifying such active peptides would not only enable additional, specific templates for biomineralization but also provide a unique view into the architecture of specific viral capsids.

1.4.7

Hydrolysis of Metal Oxides Using Peptide Nanorings as Templates

The synthesis of biominerals within the confined volumes of vesicles, microemulsions or reverse micelles elucidates a defined location for contained reactivity. Among these three systems, the constrained, ionic environment within vesicles is the most preferable microenvironment because it is not a dynamic system [37]. The biosynthesis of single-crystalline calcite within sea urchin larvae, for example, occurs inside a curved compartment with a constrained volume where the reaction is regulated by catalytically active biomolecules [37]. The high surface tensions in such confined cavities are suspected to have a considerable impact on the ensuing phase of the nanoparticle. Various research groups have used these micro- or nano-environments to provide inspiration for the confined synthesis of non-natural metal oxides by incorporating similar concepts. In the following examples, self-assembled reaction environments (peptide nanorings) were initiated by peptide monomers and metal precursor ions to yield uniform and specific phases of metal oxide nanomaterials [38, 39].

1.4.7.1 Enzymatic Peptide Nanoassembly of Crystalline Ga_2O_3

As a wide band-gap material that provides light emission over a broad range, $\beta\text{-Ga}_2\text{O}_3$ is currently being studied to exploit its potential applied, optoelectronic properties [38]. Assembled peptides were used as nanoreactors to grow the kinetically unfavored $\beta\text{-Ga}_2\text{O}_3$, which in turn provided a porous template for an efficient dehydration and water-exclusion pathway, as well as a high surface tension control that was built into the peptide cavities during the crystal growth process. This reaction was completed in a two-step process where enzymatic peptides were first assembled to template crystal growth, after which ordered single crystals were aligned through an aggregation-driven fusion. The nucleated particles were then capped by assembled peptides in solution. When the composite solution was sintered at 900°C , the peptide templates were removed and the particles transformed into an aggregated GaN phase.

Bola-amphiphile peptide monomers and (bis (*N*- α -amidoglycylglycine)-1,7-heptanecarboxylate) were used to cap and catalyze the growth of $\beta\text{-Ga}_2\text{O}_3$ nanoparticles. Such particle capping was essential in this synthesis because, in its absence, GaOOH would be synthesized (Figure 1.6). The bola-amphiphile peptide monomers were reacted with the precursor, gallium(III) chloride, for one month at pH 10, after which time both TEM and SAED were used to show that the particles displayed 50 nm diameters, and were arranged in a monoclinic crystal structure. In addition, high-resolution TEM images showed layers of the peptide surrounding the core nanoparticle.

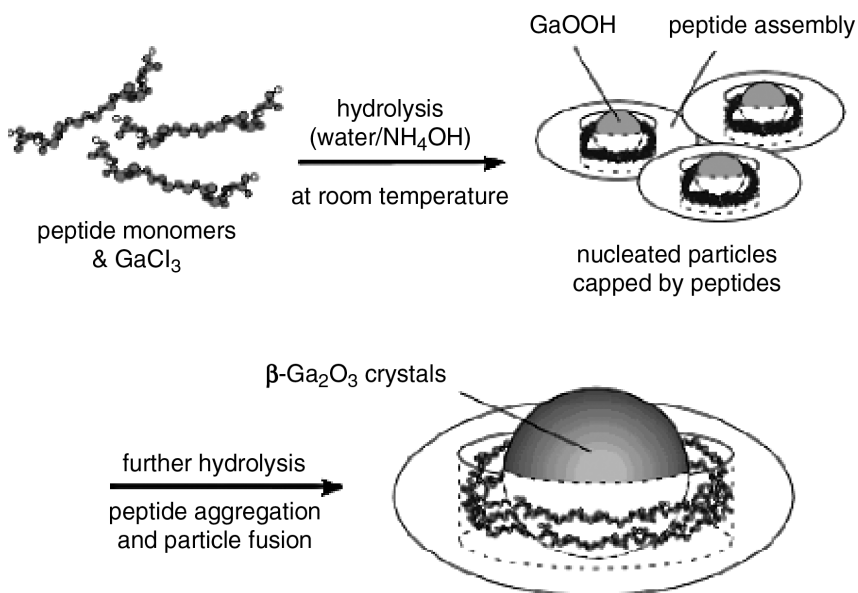


Figure 1.6 Illustration of catalytically grown $\beta\text{-Ga}_2\text{O}_3$ nanoparticles. Reprinted with permission from Ref. [38]; © 2007 American Chemical Society.

It is understood that, although the base solution hydrolyzes gallium precursors to form GaOOH, it is not strong enough to carry out the reaction, and for this reason the peptides are considered to have a catalytic function. Photoluminescence evidence confirmed the emission of the nanoparticles (389 nm), which was in agreement with previously reported values for β -Ga₂O₃. Fourier transform-infrared (FTIR) spectra subsequently indicated that the gallium hydrolysis was completed adjacent to the carboxyl and amine moieties within the assembled peptide, through a bridged metal-bridged metal complex (COO–Ga–NH²⁺). In order to investigate the importance of the nucleophilicity of this carboxyl moiety, the pH of the composite solution was adjusted to 7, and after a four-week incubation with the gallium precursor, only GaOOH crystals were observed. At neutral pH the protonated carboxyl group was shown to be weakly bound to the amine group, thus affecting the degree of gallium hydrolysis.

In addition, the importance of the bola-amphiphile template was tested. As a control, Nuraje and coworkers used the silicatein peptides that are associated with templating the hydrolysis and condensation of SiO₂ in sponge spicules. In this study, the nucleophilic hydroxyl of the serine and the primary amine from the histidine and lysine of silicatein catalyzed the hydrolysis of GaOOH and γ -Ga₂O₃ over a wide size range. Although such a wide distribution in size would limit this synthetic technique for use in industry, the control of nanoscale sizing using a specific hydrolyzing template (as for the synthesis of β -Ga₂O₃ nanoparticles) could introduce valuable properties that depend strictly on the mode of synthesis.

1.4.7.2 Synthesis of Ferroelectric BT Nanoparticles Using Peptide Nanorings

As mentioned previously, the ferroelectric and optoelectronic properties of ternary oxides such as BT can be applied to the next generation of miniaturized capacitors or random access memories [39]. In the past, BT has been synthesized at room temperature in the cubic phase, and does not exhibit ferroelectric behavior. However, Nuraje and coworkers recently reported a one-pot synthesis of ferroelectric BT in the tetragonal phase, as confirmed by electron diffraction [39]. The precursor BaTi(O₂CC₇H₁₅)[OCH(CH₃)₂]₅ was hydrolyzed by peptide templates [bola-amphiphile peptide and (bis (*N*- α -amidoglycylglycine)-1,7-heptanecarboxylate)] to produce BT nanoparticles at room temperature. When the peptide template and Ba-precursor were added together, and incubated for between one and four days in the dark, the peptide monomers were seen to self-assemble into nanorings. Atomic force microscopy (AFM) was then used to show that the BT had been synthesized exclusively within the nanoring cavity, with the average diameter (49 \pm 11 nm) of the nanorings indicating a monodisperse size distribution. Raman spectroscopy confirmed the formation of BT through a Ti–carboxylate ligation and a Ti–O–Ti stretch [39]. In order to validate this coordination, the composite solution of peptide shells was irradiated with UV light (355 nm) for 10 h, after which the peptide shells were displaced, inferring that the onset of irradiation had rendered the Ti–carboxylate linkage ineffective. Subsequently, AFM was used to identify the average diameter of the metal oxide nanoparticles alone, as 12 \pm 1 nm, after UV irradiation. Interestingly, as the pH of the peptide/precursor solution

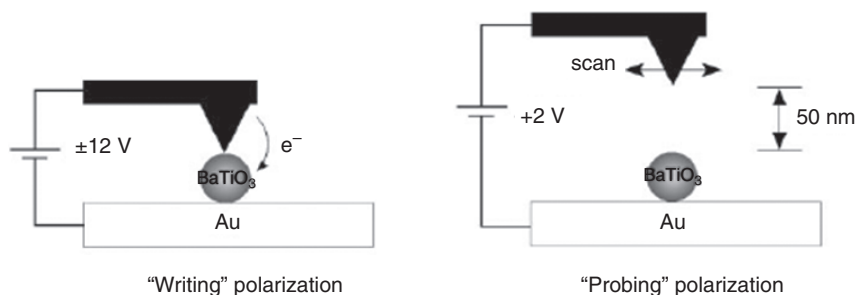


Figure 1.7 Schematic of electrostatic force microscopy (EFM). The electric potential applied to the BaTiO₃ nanoparticles using a conductive AFM tip has been varied to test its nanometer-scale ferroelectric property. In these experiments, a +12 V_{write} potential was

initially applied to the nanoparticles, and the subsequent EFM image was scanned under an applied V_{probe} potential of +2 V. Reproduced with permission from Ref. [39]; © 2006, Wiley-VCH Verlag GmbH & Co. KGaA.

changed from 4.5 to 10, the average diameter of the system fell from 49 to 23 nm, and this in turn affected the size of the resultant crystals (from 12 to 6 nm).

In order to monitor the nanoscale ferroelectric properties of BT, electrostatic force microscopy (EFM) was used to manipulate the polarization of the ferroelectric field (Figure 1.7). First, a voltage was applied to the cantilever tip (V_{write}), which gently touches the nanoparticle surface. Once the polarization has been written, the resultant polarization was probed with a lower voltage (V_{probe}) by measuring the shift in resonance of the AFM tip, using EFM. A positive applied V_{write} (+12 V) on a 12 nm particle produced a brighter contrast image than did V_{probe} of +2 V. When +12 V had been written onto the same particle, the V_{probe} was applied, and induced a darker contrast image.

1.4.8

Synthesis of ZnO from Templated Butterfly Wings

The wonderful array of colors associated with different species of butterflies often attracts the eye for aesthetic purposes only. Although used for sexual signaling or defense mechanisms (camouflage), the color of the butterfly wings is actually necessary for its survival. Designed for aerodynamics and protection, the microstructure of butterfly wing scales (which are the cuticular products of a cell) are composed of a lightweight, porous material with alternate layers of chitin and air [40]. Although the precise chemical composition of the scales is not known, chitin and the proteins resilin and scleretin have been identified within the insect cuticle. The scales are composed of long, parallel ridges that are connected by cross-ribs (1280 nm long, 380 nm wide) [41] that do not contribute to the color of the butterfly but rather offer defined regions that can be manipulated for further functionalization.

Zhang and coworkers utilized the wing's porous architecture and the terminal hydroxyl and amino moieties of surface proteins to direct the constrained synthesis

of tubular ZnO nanowires [40, 42]. Tubular materials of high porosity are understood to have properties suitable for catalysis or device storage [40]. For this process, a zinc nitrate ($\text{Zn}(\text{NO}_3)_2$) solution in ethanol was coated onto the surface of the wing after a 12 h incubation at room temperature [40], and the functionalized wing was then washed extensively with deionized water to ensure that the Zn^{2+} ions had been effectively adsorbed within the surface hydroxyl and amino groups of chitin. The wing was then placed in an oven at 500°C for 2 h, during which time the flat scales of the wings were broken apart along their stress ridges and the chitin substrate was burned. As a consequence, the calcified product yielded ZnO microtubes within the ceramic wings.

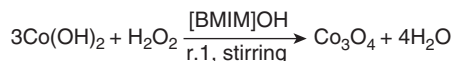
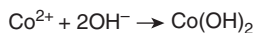
Subsequent X-ray diffraction (XRD) studies confirmed that the resultant composites had a zincite hexagonal structure, while field emission scanning electron microscopy (FESEM) was used to determine the dimensions of the microtubes produced ($3.0\ \mu\text{m}$ diameter). When the shrink ratios were calculated, the distance between the ridges and the length of the tubes was calculated to have shrunk approximately 45.7% and 41.6%, respectively, from the original template, which inferred that the microtubes had grown directly from the wing scales. Cathode luminescence from the free exciton at $3.24\ \text{eV}$ documented two emission bands ($\lambda = 381$ and $572\ \text{nm}$) of the as-synthesized ZnO. Although not confirmed, it is believed that the origin of the emission is a result of center defects of oxygen, indicating that the tubes sustain a low oxygen content, which is consistent with previous ZnO syntheses using block copolymers or solid-state conditions [40].

1.4.9

Ionic Liquid-Assisted Co_3O_4 Synthesis

As a magnetic p-type semiconductor that can be used in catalysis, sensor optimization or energy storage, Co_3O_4 has previously been synthesized using thermal decomposition, CVD or chemical spray pyrolysis of an oxidized Co product. Unfortunately, these reaction conditions are not only unfavorable for the synthesis of Co_3O_4 nanocrystals because their high-temperature reaction conditions, but they also induce a low product yield. In an attempt to overcome this setback, Zou and coworkers have used a relatively new technique incorporating room-temperature ionic liquids (RTILs) to direct the synthesis of the Co_3O_4 nanocrystals [43]. RTILs have recently attracted attention as stable, highly reactive solvents, with good electrical conductivity, high ionic mobility and good chemical and thermal stabilities [44].

In this synthesis, an ionic liquid, 1-*n*-butyl-3-methylimidazolium hydroxide ([BMIM]OH) was dissolved in $\text{Co}(\text{NO}_3)_3 \cdot 6\text{H}_2\text{O}$ at room temperature (Scheme 1.2) and, over a 30 min period, both NaOH and H_2O_2 were added separately to the solution. After a 6 h period of stirring, a black-brown precipitate was collected, purified and dried in the oven at 80°C for 10 h. The ionic liquid was collected and reused. The crystal structure of the resultant Co_3O_4 nanocrystals was determined using XRD analysis, and its composition confirmed by IR spectrometry. The diffraction peaks indicated a cubic spinel system with lattice parameters similar to



Scheme 1.2 Ionic reaction of cobalt precursor in the presence of NaOH and H₂O₂. Reprinted from Ref. [43] with permission from Elsevier.

that reported previously, while scanning electron microscopy (SEM) imaging showed the nanocrystal sizes to range from 10 to 50 nm, with a spherical appearance. These polar, ionic solvents offer a highly reactive environment because of the low interfacial tension, which induces catalysis and subsequent nucleation of the nanocrystals. When the Co-precursor has been added, the reactants disperse into the solvent to form many thousands of reactor sites that can be reused over and over again, thus providing a low-cost method for the rapid production of Co₃O₄.

1.4.10

Conclusions

While the use of metal oxide nanoparticles is dependent on their synthesis and subsequent magnetic or ceramic properties, size homogeneity is also necessary because the nanoparticles' properties are related directly to their size. Natural templates, such as butterfly scales, peptide nanorings and bacterial or protein cages, can be tuned to induce narrow size distributions that have yet to be seen within an industrial setting. These chemically engineered systems have been proven to serve as viable nanoscale templates for the constrained biomimetic synthesis of higher-ordered metal oxide nanoparticles with unique properties specific to their synthesis.

1.5

Mediated Mineralization

The structure of certain biogenic organisms is understood to be mediated by the cooperative reactivity of self-assembled macromolecules within aqueous solutions. Such hierarchical, supramolecular assemblies have revealed interesting morphological properties that can be applied directly to materials development. Diatoms and echinoderms are two independent examples of organisms that exhibit genetically controlled metal oxide structures with technologically relevant properties [31, 45]. Although progress has been made in identifying their structure-directing precursors, their complex biomineral shapes have yet to be fully recapitulated, and progress in this area is described in the following sections. By isolating the biomolecules responsible for cell wall mineralization and documenting their

reactivity, it has become possible to incorporate the specific, reactive moieties of peptide- and nonpeptide-based analogues for the biomimetic synthesis of novel nanomaterials.

1.5.1

The Three-Tier Architecture of Nacreous Layers

Mother-of-pearl (nacreous layer) possesses interesting morphological properties that are dependent on its aragonite–biopolymer coordination. Evidence has suggested that these biopolymers are incorporated into the composite framework of the mineral and are responsible for inducing different morphological properties of the organism [29]. Electron microscopy has been used to characterize these hybrid composites, and has shown that the macroscopic periodic orientation of the nacreous layer is assembled through a three-tier process of repetitive growth, inhibition, and regrowth [29]. The layered aragonite composites (tier 1) have been predicted to be perfectly aligned through a series of mineral bridges (tier 2) (1–5 μm wide and 200–700 nm thick). These bridges are assembled by nanobuilding blocks (tier 3) that have aggregated into hexagonal plates (Figure 1.8) [29].

Non-natural mimics of the assembled nacreous layer have been synthesized, displaying similar nanoscale architectures under ambient conditions. In these studies, the biomimetic crystallization of host organic molecules, generated

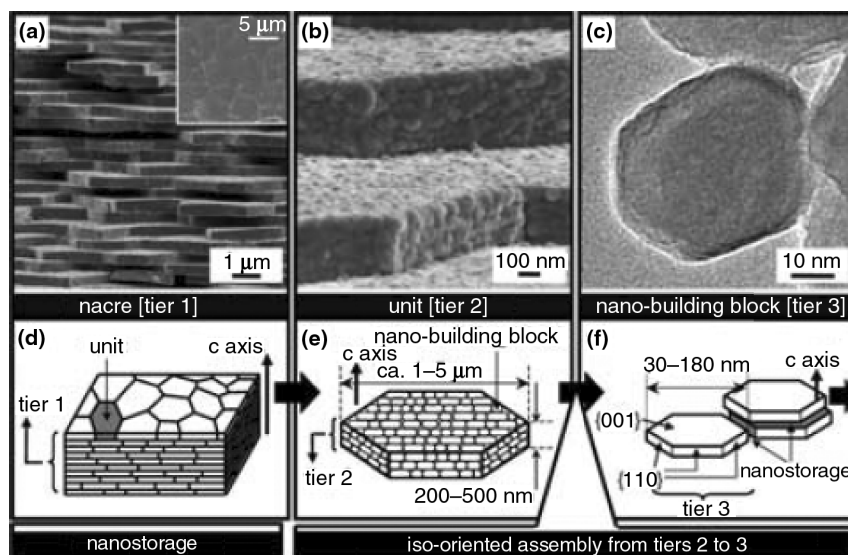


Figure 1.8 The three identified tiers of the nacreous layer. (a,b) FESEM images and (c) FETEM image; (d–f) Schematic representations of tiers 1, 2 and 3, respectively. Reproduced with permission from Ref. [29]; © 2005, Wiley-VCH Verlag GmbH & Co. KGaA.

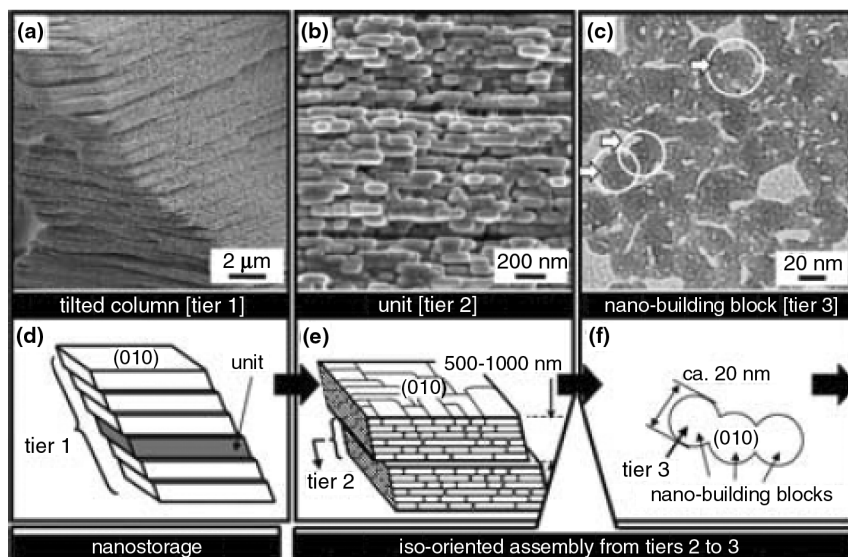


Figure 1.9 The three identified tiers of the K_2SO_4 -PAA biomimetic assembly. (a,b) FESEM images; (c) FETEM image; (d–f) Schematic representations of tiers 1, 2 and 3, respectively. Reproduced with permission from Ref. [29]; © 2005, Wiley-VCH Verlag GmbH & Co. KGaA.

through a potassium sulfate (K_2SO_4) and poly(acrylic acid) (PAA) composite reaction, were shown spontaneously to form three-tier assemblies. Electron microscopy revealed that tier 1 consisted of an assembly of plates composed of square units (tier 2), approximately $0.5\text{--}1.0\ \mu\text{m}$ thick. However, when magnified at a higher resolution these squares were shown to originate at nanoscale defect sites that were bridged by $20\ \text{nm}$ building blocks (tier 3) (Figure 1.9). The physical properties associated with these packed, nanoscale building blocks were probed using photoluminescence, whereby hydrophobic and hydrophilic organic dyes were encapsulated within the defect sites of the three-tier matrices. After time, an examination of the photoluminescence showed that the stored dyes were still actively fluorescing, potentially providing an interesting source for molecular storage.

1.5.2

Echinoderms

The three-tier assembly documented for mother-of-pearl can be extended to the nanoscale architectures of other mineralized organisms. The sponge skeletal organization of echinoderms, for example, is composed of calcitic nanobricks of one, single Mg-bearing calcite crystal. Three species of echinoderms and one shell of a sea urchin were analyzed using FESEM, field emission TEM (FETEM), SAED

and XRD [31]. Although the organic composite membrane of the shells could be extracted using an aqueous solution of sodium hypochlorite (5% NaClO), the biopolymer remained associated specifically to the remaining rhombohedral calcite crystals. The nanobricks (submicron domains) of occluded biological macromolecules exposed on the cell surface of echinoderms were shown to be interconnected through a series of defined bridges at their nanoscale defect sites, similar to those found on nacreous layers [31].

The crystalline, calcitic domains of echinoderms were studied on a molecular level and shown to be electrostatically driven by assemblies of biomolecules with carboxy moieties. In fact, Addadi and coworkers have identified biological molecules associated with the sea urchin spine as water-soluble proteins, rich in aspartic and glutamic acid [46]. These amino acids were proposed to occupy the boundary sites between the crystalline domains of the nanobricks, inducing a necessary electrostatic environment for further reactivity. Similar to nacreous layers, the nanobrick growth of echinoderms is initiated along the defect sites of the biopolymer/nanobrick interface, thus exposing potential molecular storage units (Figure 1.10). The reported literature on the biopolymer-mediated synthesis of tightly packed nanobrick layers within species of echinoderms can be applied to the bioinspired synthesis of non-natural metal oxides.

1.5.2.1 Biomimetic Synthesis of Metal Oxides Using Echinoderms as Inspiration

By utilizing the fundamental Lewis acid and base interaction, defined organic molecules were used in conjunction with appropriate precursors under variable conditions to rapidly precipitate nanoparticles with constrained sizes. Specifically, mosaic assemblies of nanowires of ZnO and nanocrystals of Mn_3O_4 and $\text{Co}(\text{OH})_2$ were synthesized using different polymeric backbones [30, 47]. The mosaic assemblies within these metal oxides are initiated from the nanocrystals themselves and, as seen in echinoderms and nacreous layers, these materials were grown, inhibited and regrown at the defect sites of bridged nanocrystals. In these reactions, the incorporated polymeric backbone generated an electric dipole moment that induced an internal self-assembly of the primary crystals *in vitro*; these assemblies were then reorganized into a highly specific metal oxide crystal structure with functional properties.

1.5.2.1.1 Nanoscale Building Blocks for ZnO Nanowires Interesting properties associated with one-dimensional (1-D) zinc oxides can be employed in both electronic and optoelectronic applications [30]. Previously synthesized using vapor-phase thermal evaporation, wurtzite-type ZnO has potential applications which range from gas sensors to varistors, because of its wide-bandgap semiconducting properties. The 1-D lateral growth of ZnO is especially significant because it can be used as an ultrasensitive biochemical detector or field-effect transistor. For this reason, a low-temperature synthesis was developed to optimize the production of ZnO for such applications. The resultant synthesis produced 1-D mosaic structures reminiscent of the molecular architecture of echinoderms [30].

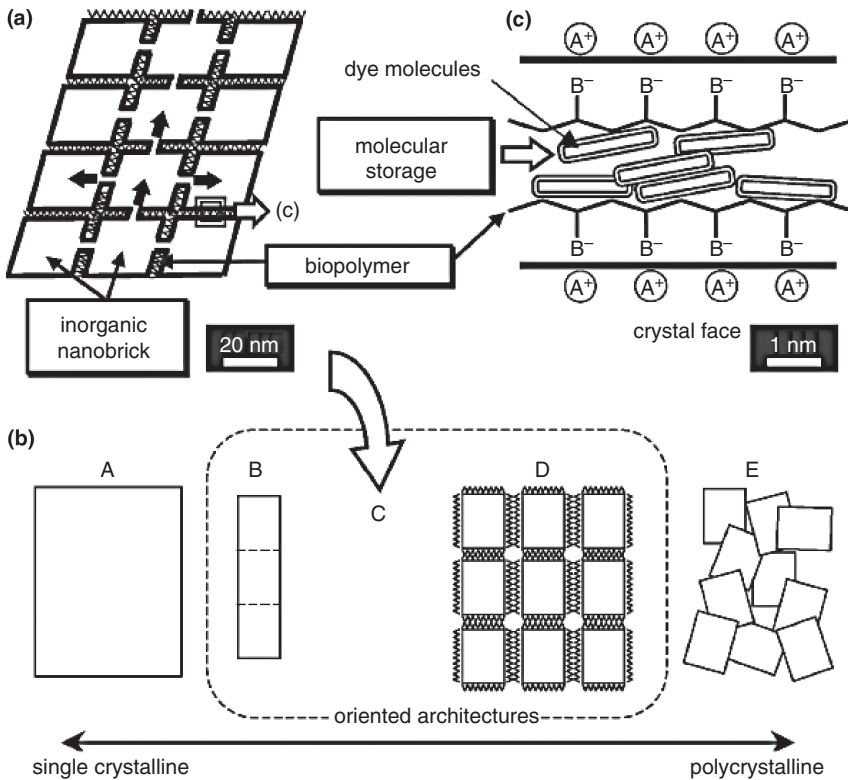


Figure 1.10 Schematic of nanoengineered nanobricks of nacreous layer and echinoderms. (a) Nanobricks oriented involving nanobridges; (b) Schematic of oriented architectures from single crystalline (A) to oriented attachment (B–D); (c)

Interaction between the nanobricks and biopolymers producing the emergence of molecular storage and (E) polycrystalline arrangement. Reproduced with permission from Ref. [31]; © 2006, Wiley-VCH Verlag GmbH & Co. KGaA.

Yahiro and coworkers prepared this synthesis using an aqueous solution of zinc heptahydrate ($\text{ZnSO}_4 \cdot 7\text{H}_2\text{O}$) and ammonium chloride (NH_4Cl) at fixed molar ratios. The pH was adjusted to 9.5, and again to 11, using NaOH. Pyranine (8-hydroxy-1,3,6-pyrenetrisulfonate) was added in various molar ratios (Figure 1.11), after which the solution was aliquoted onto glass slides for ZnO film nucleation and growth and incubated for 24 h at 60 °C. The resultant slides were characterized using electron microscopy.

The anionic pyranine molecule was expected to direct the lateral growth of ZnO nanowires on a two-dimensional (2-D) surface [30]. Control studies with an absence of pyranine induced nanorods of wurtzite ZnO that grew vertically along the c-axis, as characterized by XRD analysis. At low molar ratios of pyranine, c-axis-oriented nanorods were also formed, but in hexagonal patterns; in contrast, at high molar ratios of pyranine the oriented growth became laterally elongated, extending in a desirable direction across the substrate. An electron energy-loss spectroscopic

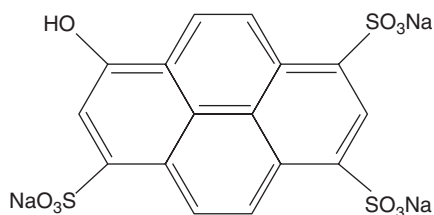


Figure 1.11 Structure of pyranine. Reproduced with permission from Ref. [30]; © 2006, Wiley-VCH Verlag GmbH & Co. KGaA.

(EELS) analysis suggested that the pyranine had become wrapped around the developing nanowires during the synthesis, while both energy-filtered (EF) TEM and high-frequency (HF) TEM analyses indicated that, during the aqueous synthesis, the pyranine molecules had been incorporated into the growing ZnO matrix by adsorbing to the faces of the hexagonal ZnO lattice points, thus inhibiting crystal growth perpendicular to the *c*-axis.

A closer examination of the composition, using high-angle annular dark-field scanning transmission electron microscopy (HAADF-STEM), showed that the nanowires were actually composed of nanograins (5.8 nm grain size, based on XRD peaks). The interior granular structures were understood to be composed of bridged nanocrystals that were oriented by the pyranine molecules, which inferred that the pyranine precursor was essential for the mediated synthesis of ZnO nanowires. Because there was no evidence of branching wires during the growth process, the 1-D morphology could be attributed to an anisotropic growth of a weak seed particle that bridged adjacent particles together. Hence, pyranine not only induced an electrostatic environment that enabled the assembly of structured ZnO nanograins, but also oriented ZnO growth, producing an ordered arrangement of nanowires on the 1-D scale.

1.5.2.1.2 Manganese Oxide and Cobalt Hydroxide Manganese and cobalt materials are technologically important as electrochemical, magnetic and catalytic metal oxides. Oaki and coworkers have developed a biomimetic synthesis, incorporating PAA to template manganese oxide and poly(ethyleneimine) (PEI) to template cobalt hydroxide nanoflakes with interior mosaic structures [47]. Previously, manganese oxide nanocrystals have been synthesized using a solid-state reacted precursor [48], while other syntheses have produced plate and sheet-like morphologies of manganese oxide with submicron feature sizes. As an alternative approach, a 1-D polymer template was used to demonstrate a controlled, room-temperature synthesis of both manganese oxide and cobalt hydroxide. By utilizing these templates, the resultant nanoparticles were built from the bottom up and exhibited an internal hierarchical assembly of mosaic nanocrystals, similar to structures seen in echinoderms.

A mixture of manganese chloride tetrahydrate ($\text{MnCl}_2 \cdot 4\text{H}_2\text{O}$) and PAA immediately formed a clear orange liquid that became turbid after several hours of

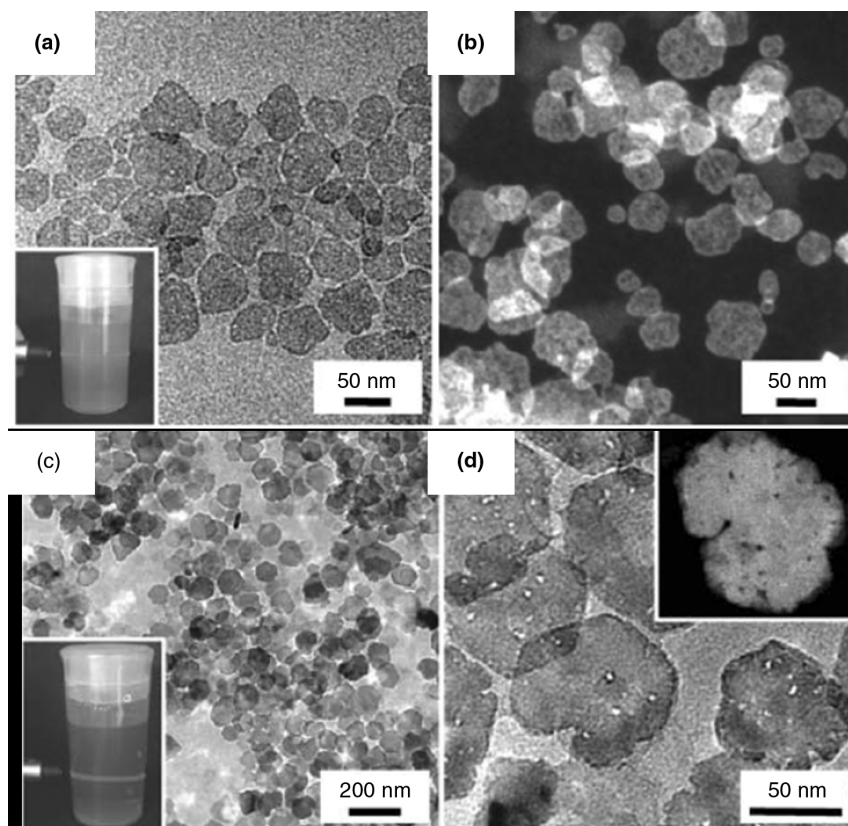


Figure 1.12 Overview of manganese oxide and cobalt hydroxide nanoflakes. (a,b) Manganese oxide with (a) FETEM image and Tyndall light scattering inset and (b) HAADF-STEM image of magnified flakes; (c,d) Cobalt hydroxide nanoflakes with (c) FETEM image and dispersed inset and (d) HAADF-STEM of mosaic structure. Reproduced from Ref. [47], by permission of the Royal Society of Chemistry.

mixing. Both, FETEM and HAADF-STEM showed that the particles in solution were actually hexagonal nanoflakes on the order of 50 nm and composed of 2–3 nm nanograins (mosaic structure) with an approximate 10 nm thickness (Figure 1.12a,b). The presence of manganese oxide was confirmed by energy-dispersive X-ray (EDX) analysis, while HRTEM and FFT suggested a birnessite crystal lattice composed of edge-shared MnO_6 octahedrons. A dispersed liquid film of Mn_3O_4 was drop-cast onto a silicon wafer, and an FT-IR spectrum collected. The results indicated that the mosaic interior of the birnessite-type manganese oxide contained a PAA-controlled crystal structure in the presence of sodium ions.

A similar synthesis incorporating cobalt chloride hexahydrate ($\text{CoCl}_2 \cdot 6\text{H}_2\text{O}$) and PEI produced a reddish-yellow composite solution that was shown to be composed of hexagonal nanoflakes that were less than 100 nm in size. Both, FETEM and

FESEM were used to identify the rough features of the nanoflakes, which were shown to be approximately 10 nm thick and composed of 5 nm crystals (Figure 1.12c,d).

An EDX analysis confirmed the composition of $\text{Co}(\text{OH})_2$ -PEI containing traces of sodium ions and water molecules in between the monolayers of a brucite-type crystal lattice. Finally, SAED, HRTEM, FFT, XRD and FT-IR were each used to confirm that the material was composed of octahedral coordinated cobalt nanoflakes with intercalated sodium ions in a brucite-type structure.

The results from both syntheses have indicated that tailoring the polymer template for a specific metal precursor could yield functional nanomaterials with highly controlled properties. The nanoflakes of manganese oxide and cobalt hydroxide were synthesized with mosaic interiors that were ascribed to a stepwise crystal growth. Similar to the formation shown in Figure 1.11, this growth can be understood as a series of inhibitions and regrowths at the defect sites, as demonstrated previously for the echinoderms.

1.5.3

Diatoms

In Nature, diatoms represent one of the largest groups, and perhaps one of the most studied single-celled eukaryotic microalgae found in almost every seawater and freshwater habitat. These microorganisms have silica-based cell walls, which range in size from ~50 to 500 nm (Figure 1.13) [49]. Although diatom silica is X-ray amorphous, it still exhibits highly regular and rather exquisite patterns of pores, ridges or tubular structures that are formed under genetically controlled processes. Studies using electron microscopy have revealed that the valves and girdle bands associated with silica formation are formed inside the cell, within highly specialized membrane-bound compartments called silica deposition vesicles (SDVs) [50]. When morphogenesis has been completed, these silica species are deposited on the cell surface using SDV exocytosis.

Currently, microelectronics relies on bulk silica as an important dielectric material that is often used as an insulating template for further reactivity. On the nanoscale, silica can be synthesized by polymerizing silicic acid in an aqueous system, or through hydrolysis and condensation of silicon alkoxides in the Stöber synthesis [51]. The mechanism of these two methods is unique. The first method is dominated by monomers and tetra-functionalized species, such that the resultant silicate sols are uniform, which means that they are fully hydrolyzed and grow by monomer addition. In contrast, for the second method, di- and tri-functionalized species are dominant for alkoxides. Regardless of the synthesis used, these particles induce a fractal interior with minimal morphological control due to their common template, ammonium hydroxide [51].

In Nature, specific silicon transport proteins (SITs) produced by diatoms are responsible for the uptake and delivery of orthosilicic acid ($\text{Si}(\text{OH})_4$, $\text{p}K_a = 9.8$) to the diatom. Within the cell, orthosilicic acid is then concentrated up to 1000-fold, resulting in the condensation of amorphous, hydrated silica [45]. Strikingly, the

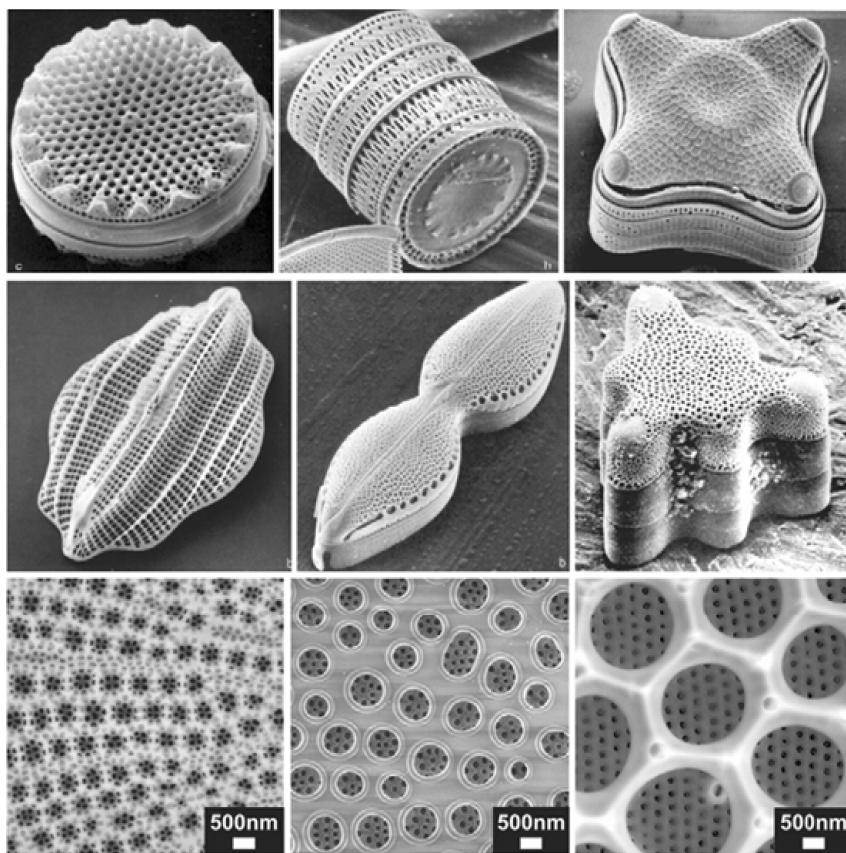


Figure 1.13 Scanning electron microscopy images of the cell walls of a variety of diatom species. Reprinted from Ref. [45], with permission from Elsevier.

polycondensation of silica occurs in neutral to slightly acidic pH conditions, under ambient temperatures and pressures. Although these conditions are considered mild, diatoms still have control over the product morphology. It is understood that the patterns created by diatoms are species-specific, and consequently their directed growth process must be regulated in a genomic manner [51].

Recently, significant effort has been devoted to determining the specific templates used by different species of diatoms in silica formation. Although, diatom cell walls consist primarily of silica doped (~97%) with trace amounts of aluminum and iron, they also contain a wide variety of incorporated organic molecules and proteins [52]. In fact, solid-state nuclear magnetic resonance (NMR) spectroscopy has revealed that some of these molecules and coat proteins are encapsulated within the silica matrix [53, 54]. Two main templates for silica growth were identified after dissolution of the silica cell wall with hydrogen fluoride (HF) or ammonium fluoride. In the following sections, we will show how these templates have been

optimized and utilized for further reactivity, thereby revealing interesting properties that are directly applicable to the synthesis of novel nanomaterials.

1.5.3.1 Biological Synthesis of Silica Nanoparticles

Extracted and purified from up to three species of diatoms (*Cylindrotheca fusiformis*, *Thalassiosira pseudonana* and *Eucampia zodiacus*), silaffins are polypeptides (4–17 kDa) with a variety of post-translational modifications, including propylamino-functionalized lysine side chains (Figure 1.14) [49]. Currently, four silaffin genes have been identified (one from *C. fusiformis* [*sil1*] and three from *T. pseudonana* [*tpSil1*, *tpSil2* and *tpSil3*]), which encode for eight known polypeptides. Of these four genes, only *tpSil1* and *tpSil2* have shown sequence similarities, likely from gene duplication; however, the overall lack of sequence similarity strongly suggests that the post-translational modifications of silaffins are critical to their function. These post-translational modifications include the monohydroxylation of lysine and proline, dihydroxylation of proline, *o*-phosphorylation of serine, threonine, hydroxyproline and hydroxylysine, glycosylation, sulfation of carbohydrate moieties, and the alkylation of ϵ -amino groups of lysine [52, 55]. These modifications are charged and stabilized through electrostatic interactions between the phosphate groups on one silaffin to the charged amines of another, inducing a self-assembled template available for further reactivity.

The different structures associated with different species of diatoms are directly related to the silaffin being studied. For instance, spheres (silaffin-1/2L mixture from *T. pseudonana* [56]), dense plates (silaffin-3 from *T. pseudonana* [56]) or porous sheets (silaffin-1/2H mixture from *T. pseudonana* [56] or natSil-2 from *C. fusiformis* [57]) are all a function of a precursor template. While silaffins are responsible for controlling which shapes are formed in the SDV, positively charged long-chain polyamines (LCPAs) are an integral part of silica condensation [45]. Those silaffins that are negatively charged must be stabilized by the LCPAs, or the

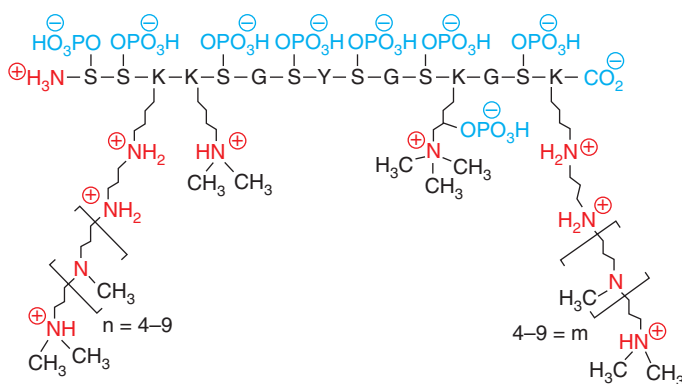


Figure 1.14 Chemical structure of silaffin-1 A_1 from *C. fusiformis*. Reproduced with permission from Ref. [55]; © 2006, Wiley-VCH Verlag GmbH & Co. KGaA.

recently discovered silacidins [58] (in *T. pseudonana*), to complete silica condensation.

The LCPAs are nonprotein components (>3.5 kDa) that have been found encapsulated in the silica matrix of the diatom, and isolated through a series of HF extractions [59]. Unlike silaffins, which have a peptide backbone, these polyamines consist of linear chains of C–N-linked PEI units that are bonded to a putrescine or putrescine derivative backbone. The chemical composition of these LCPAs is unique for each diatom species, with variable repetitions and degrees of methylation.

Similar to the reactivity of silaffins, silica production in the presence of LCPA and silicic acid requires an addition of counteranion in the form of phosphate, sulfate or citrate ions. This electrostatic matrix is projected to induce the formation of silica by the microscopic aggregation of LCPAs and subsequent phase separation into a LCPA–anion-rich microdroplet [50]. In his 2002 theory of cell wall morphogenesis, Manfred Sumper suggested that the formation of secondary patterns, as seen on the diatom cell wall, is related to the wall-to-wall distance of the areolae, hexagonally packed polyamine monolayers and the polyanion concentration, on the surface of the SDV [14]. For example, a size-control experiment using LCPAs from *Stephanopyxis turris* has shown that the size of nanoparticles was dependent not only on the phosphate concentration but also on whether orthophosphate or a more highly charged pyrophosphate was used [60].

The biological mechanism of diatom silica formation has been demonstrated as a valuable source for bioinspired templates for non-natural metal oxide synthesis at ambient temperatures and near-neutral pH. Moreover, silica nanostructures can be tuned according to a specific template, providing functional properties that can be directly applied in the design of nanomaterials. These syntheses have integrated moieties that are tuned for a specific function, such as the encapsulation of functional enzymes [61, 62] and controlled construction of nanomaterials through nanoscale building blocks [63–65]. Thus, we will focus here on how these synthetic strategies control and optimize silica formation, and how such materials can (potentially) be used in a variety of applications.

1.5.3.2 Biomimetic Synthesis of Silica Nanoparticles

Mimicking the nanopatterns of the diatom cell wall remains a major challenge for materials scientists because the natural reaction mechanism is still unknown, with many essential components for silica precipitation yet to be discovered. However, it is well known that the terminal amine templates interact with monosilicic acid to induce the specific morphology of the resultant silica. A variety of different silica precursors have been used with a number of templates, including tetramethyl orthosilicate (TMOS) [62, 66–73], tetraethyl orthosilicate (TEOS) [63, 74, 75], tetrakis(2-hydroxyethyl) orthosilicate (THEOS) [74], sodium silicate [65], a silicon–catechol complex [64, 76] and dipotassium tris(1,2-benzenediolato-*O,O'*) silicate [77]. In addition, a variety of bioinspired templates have been used, including synthetic and natural polypeptides [63, 66, 75], polyamines [68, 73, 76], and even modified organic materials, including cellulose [74] and chitosan [78].

Recently, synthetic or natural polypeptides have been created or modified to serve as silica condensation templates. Examples of these include the poly(amino acids) [79], the diatom-derived R5-peptide [66], chimeric polypeptides [64, 67], block copolypeptides [71, 72, 75, 80], lanreotide [63] and even the naturally occurring protamine [65]. These polypeptides have been used to produce a variety of silica shapes and sizes, which can be tuned to perform a variety of applications, including transport and the separation of encapsulated materials [62], or potentially for drug delivery [73].

1.5.3.2.1 Block Copolypeptides Block copolypeptides, which have been used as templates for controlled silica formation [71, 72, 75, 80], consist of covalently linked domains (domains) of hydrophilic and hydrophobic polypeptides. Due to their unique polarities, these block segments induce an amphiphilic character, resulting in self-assembled vesicles in aqueous solution [75]. For example, a copolypeptide consisting of polymers of linked lysine and glycine residues (*Lys-b-Gly*), was used as a silica template in the presence of orthosilicic acid and phosphate buffer at pH 7.2 [72]. Different methods of silica precipitation were tested by changing the amount of silica precursor or the amount of phosphate present during precipitation. In Method I, 6 mmol of silica precursor was used, while in Methods II and III 30 mmol was used. In addition, Method III included 7.5 mmol more phosphate buffer than the other two methods (0.1 M). An increase in phosphate buffer (Method III) resulted in a spherical morphology (40–120 nm diameter), while the other two methods produced mostly platelets for the *Lys-b-Gly* block copolypeptides (Table 1.1).

The formation of platelets or spheres with the *Lys-b-Gly* copolypeptide suggested that there was a morphological dependence on the phosphate concentration and solubility of the hydrophobic block. As the relative hydrophobicity was increased though the addition of Gly residues, substitution of the Gly block with the more hydrophobic Ala block, or the loss of Lys residues, the solubility of the copolypeptide was decreased, making it more susceptible to phase separation. The hydrophobic block was more energetically stable when it was associated, rather than by

Table 1.1 Silica morphology for each copolypeptide at different synthesis conditions.

Co-polypeptide	Morphology (Methods I, II)	Morphology (Method III)
<i>Lys</i> ₂₀₀ - <i>b-Gly</i> ₅₀	Platelets	Spheres
<i>Lys</i> ₃₄₀ - <i>b-Gly</i> ₈₅	Platelets	Spheres
<i>Lys</i> ₁₁₀ - <i>b-Gly</i> ₅₅	Spheres and platelets	Spheres
<i>Lys</i> ₃₂₀ - <i>b-Gly</i> ₁₆₀	Platelets	Spheres
<i>Lys</i> ₄₀₀ - <i>b-Ala</i> ₁₀₀	Spheres	Spheres
<i>Lys</i> ₃₉₀ - <i>b-Ala</i> ₆₅	Spheres	Spheres
<i>Lys</i> ₄₅₀	Platelets	Platelets

Reproduced with permission from Ref. [72]; © 2007, Wiley-VCH Verlag GmbH & Co. KGaA.

being free in solution, so aggregation of this region was induced and the condensation of spherical silica was promoted, rather than platelets. In addition, an increase in phosphate ions (Method III) had a similar effect by electrostatically interacting with the hydrophilic lysine block and promoting silica sphere production. Thus, by optimizing the hydrophobicity of the template and the phosphate concentration, specific morphologies could be obtained. In addition, the platelets from Method II were smaller than those from Method I, as a result of the higher concentration of silica precursor and subsequent increase in the rate of nucleation (Figure 1.15).

Cyclic lanreotide is a dicationic octapeptide that self-assembles into nanotubes in water with a monodispersed diameter of 24.4 nm and a wall thickness of 1.8 nm [63]. This polypeptide has two exposed protonatable amine groups that can be used as catalytic sites for silica condensation (Figure 1.16).

By exposing the nanotubes to a TEOS-derived $\text{Si}(\text{OR})_3\text{O}^-$ precursor, silica was deposited and bundles of silica nanofibers were formed with a total length up to 7 μm , and each nanotube extending up to 3 μm . A TEM analysis determined that the dried fibers consisted of bundles of aligned nanotubes with homogeneous inner and outer diameters of 14–16 nm and 28–30 nm, respectively. In addition, the two concentric tubes were both 1.4 nm thick, and separated by 2 nm, which is the approximate width of the lanreotide molecule. The proposed dynamic templating mechanism suggested that the cationic lanreotide nanotube surface catalyzed the silica condensation by electrostatic forces, and the consequent anionic silica deposits promoted additional lanreotide assembly through synergetic neutralization of the entire system (Figure 1.17).

Not only does this templating mechanism provide insight into the potential fundamental mechanisms used in biological systems, but it also allows for the production of superstructures that greatly exceed the size of the original template [81]. Consequently, a variety of new silica structures can be synthesized that maintain nanoscale properties even in the microscale or larger.

1.5.3.2.2 R5 Peptide The R5 peptide ($\text{H}_2\text{N-SSKSGSYSGSKGSKRRIL-CO}_2\text{H}$) is an unmodified biomimetic analogue of the silaffin precursor peptide (sil1p) in *C. fusiformis* that exhibits silica condensation activity at neutral pH in a buffered phosphate–citrate solution [13]. Several enzymes have been encapsulated within the silica matrix with the R5-peptide as the silica template, including catalase, horseradish peroxidase and butyrylcholinesterase [61, 66]. The silica matrix provides an inert cage around the enzyme, which not only protects it from the surrounding environment and increases its shelf life, but also provides the basis for biosensors and catalysts. In fact, it is not only enzymes that have been encapsulated—CoPt and CdSe and ZnS nanoparticles have also been successfully encapsulated into the silica matrix [61]. These magnetic nanoparticles may serve a wide variety of applications, including catalysis, biological labeling and detection and electronics [69]. In addition, the encapsulated magnetic particles have potential use in enzyme encapsulation, as they might provide a physical means for separating the enzyme from the reaction mixture.

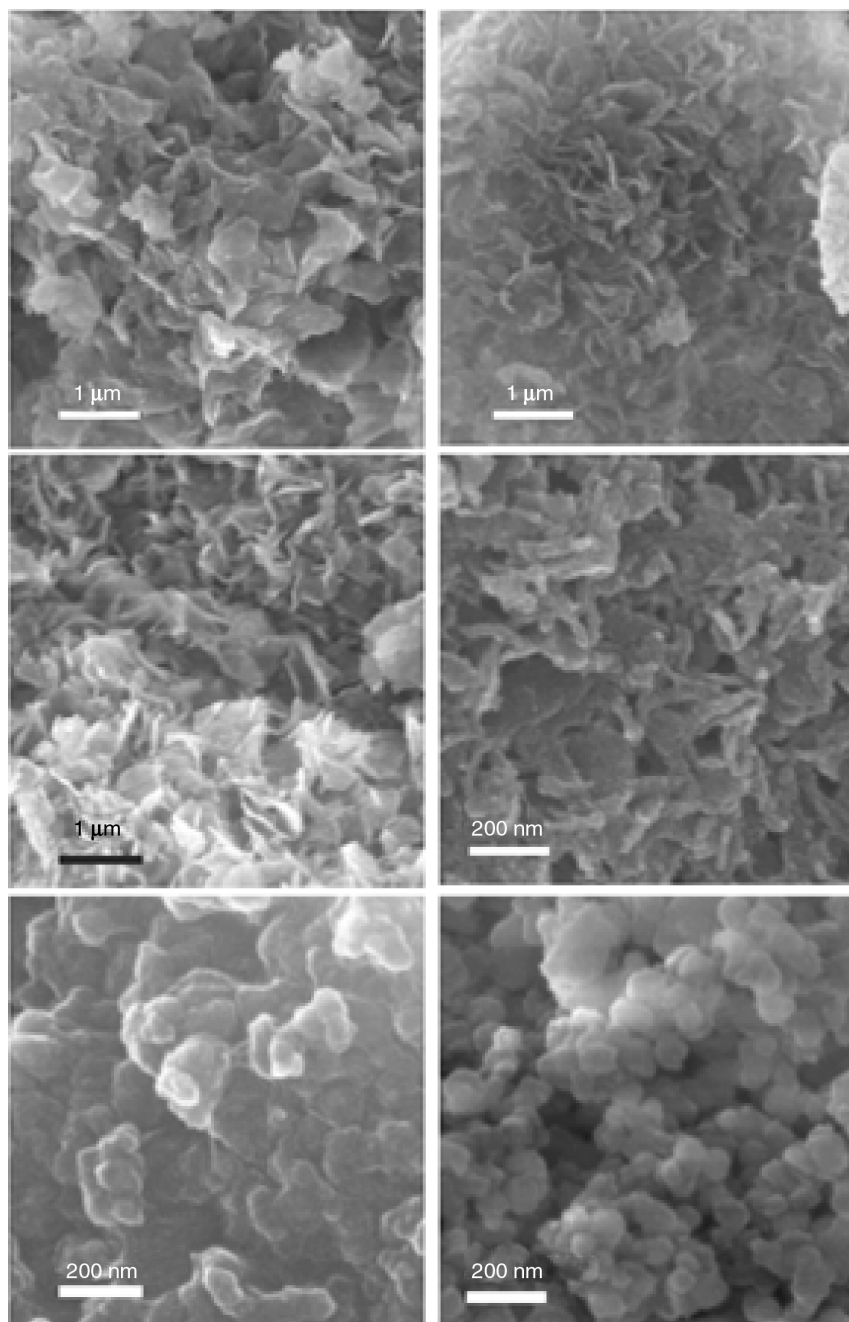


Figure 1.15 Field-emission scanning electron microscopy images of silica nanoparticles synthesized using (left) $\text{Lys}_{340}\text{-b-Gly}_{85}$ and (right) $\text{Lys}_{320}\text{-b-Gly}_{160}$ using (top to bottom) Methods I, II and III respectively. Reproduced with permission from Ref. [72]; © 2007, Wiley-VCH Verlag GmbH & Co. KGaA.

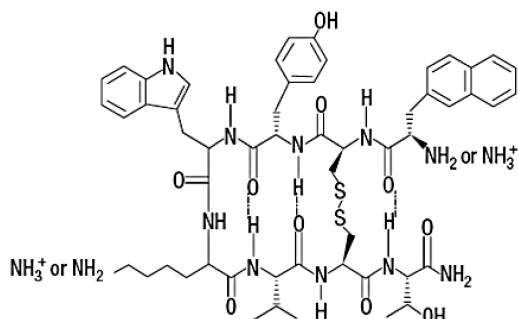


Figure 1.16 Structure of lanreotide showing the two charged amine sites responsible for silica condensation. Reprinted from Ref. [63] by permission from Macmillan Publishers Ltd.

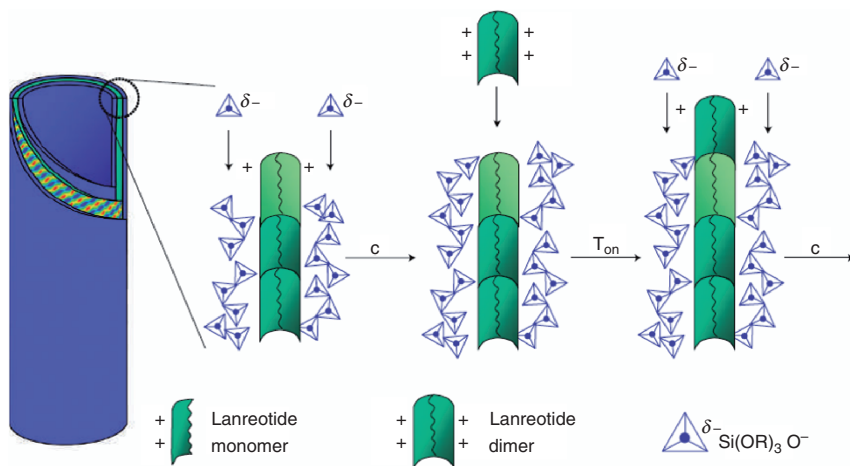


Figure 1.17 Dynamic templating model for the mechanism of silica condensation into nanofibers. The cationic lanreotide nanotube surface utilizes electrostatic attraction to catalyze silica condensation (step C) and the anionic silica deposit promotes additional lanreotide assembly (step T_{on}) through neutralization of the system. Reprinted from Ref. [63] by permission from Macmillan Publishers Ltd.

Chimeric (fusion) proteins that incorporate the R5 peptide have been synthesized to control and precipitate silica nanoparticles. Po Foo and coworkers have utilized a two-component chimeric protein consisting of the R5 polypeptide (from *C. fusiformis*) and the self-assembling domain based on the consensus repeat in the major ampullate spidroin protein 1 (MaSp1) of *Nephila clavipes* spider dragline silk [64]. MaSp1 forms highly stable β -sheet secondary structures that can be spun into intricate fibers which, when fused with the silica-templating R5-peptide, allow for the formation of film-like and fibrous silica structures (Figure 1.18).

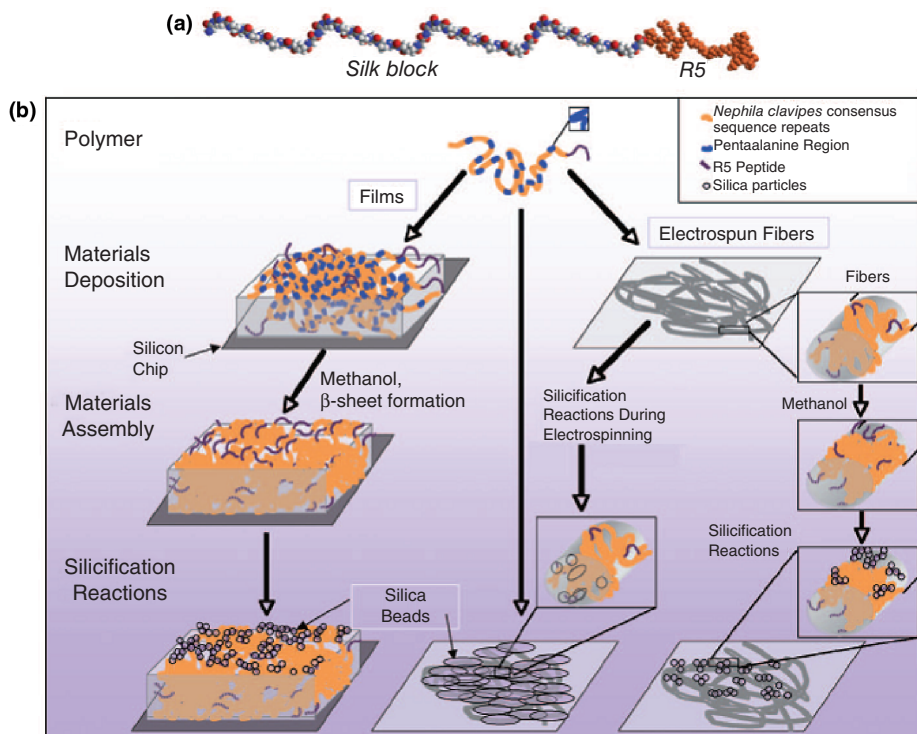


Figure 1.18 Schematic representation of the fusion protein and its use in controlled silica nanomaterial formation. (a) Schematic of the chimeric polypeptide consisting of the R5 and silk polypeptides; (b) Model of R5-silk polypeptide processing into films and fibers and subsequent silicification reactions. Reproduced from Ref. [64]; © 2006 National Academy of Sciences, USA.

Two different silk motifs were investigated, one with and one without a cell-binding motif. When silica precipitation was conducted under ambient temperatures and near-neutral pH with ratios of Si : N = 22 : 1 in solution, silica nanospheres with $>1\ \mu\text{m}$ diameter were synthesized for both fusion proteins. Thermal analysis determined that $\sim 90\%$ of the material was the templating protein and 10% was silica. Nitrogen absorption analysis showed pore radii $<10\ \text{\AA}$ and low surface areas ($\sim 10\ \text{m}^2\ \text{g}^{-1}$), which are smaller than the R5-peptide-templated silica nanospheres (pore radii $35\ \text{\AA}$, surface area $600\ \text{m}^2\ \text{g}^{-1}$). Although silica precipitation was successfully conducted with the free R5-silk peptide in solution, the silk moiety provides a means for size and shape control for the growing silica nanocomposite. When these chimeric proteins were spun into fibers via electrospinning, silica nanospheres were formed with much smaller diameters (200–400 nm). In addition, when the chimera CRGD15mer + R5 was electrospun concurrently with the silica condensation reaction, silica was deposited in and on the fibers, resulting in elliptically shaped silica particles that were fused to the fibers. As a result, processing

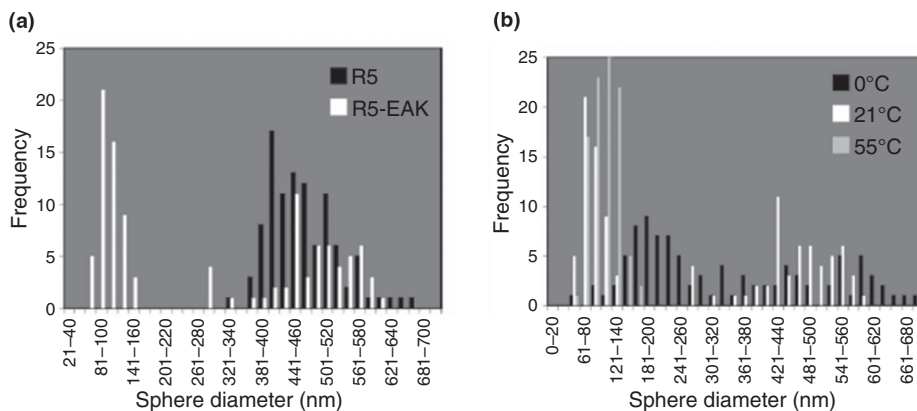


Figure 1.19 (a) Sphere diameter distribution for silica particles precipitated using R5 peptide (black) and R5-EAK₁ (white); (b) Sphere size distribution for silica particles formed with R5-EAK₁ at different temperatures. Reprinted with permission from Ref. [67]; © 2008, American Chemical Society.

modifications can be tailored to structural templates, inducing silica nanoparticles of specific sizes and morphologies. Most importantly, as this reaction is conducted under mild conditions, these fibers have a variety of potential applications in specialty materials, including those used in the biomedical field [64].

Another chimeric polypeptide consisting of the R5-peptide and a self-assembling hydrophobic-phobic (HP) protein monomer capable of self-assembly was also used to direct silica precipitation *in vitro* at neutral pH and ambient temperatures [67]. The HP monomer consisted of an n-AEAEAKAKAEAEAKAK-c sequence, called EAK₁. These monomers self-assemble into stable β -sheet supra-molecular structures due to their binary patterns, and this leads to hydrophobic and hydrophilic faces, where favorable side-chain interactions result in aggregation through hydrophobic and electrostatic interactions, respectively. Thus, an EAK₁-R5 chimeric polypeptide assembles into fibrous aggregated hydrogels and precipitates silica nanospheres with sizes that are dependent on the reaction temperature (Figure 1.19).

The size distribution of the control R5 template for silica formation produced a distribution of nanoparticles in the diameter range of 402 to 530 nm, as opposed to the R5-EAK templates, which showed a bimodal range of diameters from 63 to 103 nm and from 385 to 541 nm, respectively. However, at higher temperatures, the R5-EAK₁ peptide promoted rapid nucleation, resulting in a loss of bimodal character and subsequently the production of smaller silica nanoparticles (64–116 nm diameter). Not only does the change in diameter size with different temperatures allow for the production of size-specific tailored silica nanocomposites, but the loss of bimodal character at a higher temperature also allows for an even tighter control of the silica structure under these conditions. By adjusting this morphology under mild reaction conditions, biologically active matrices can be

synthesized and perhaps used in solid-state enzymatic catalysis, physiologically active biomatrix implants and, potentially, also biosensors [67].

1.5.3.2.3 Poly-L-Lysine Poly-L-lysine (PLL) has been implicated in silica formation because of its ability to adopt an α -helix, β -sheet or random coil conformation. PLL is an excellent silica template due to its ability to create different silica morphologies by simply changing the reaction conditions to afford a specific secondary structure. Hawkins and coworkers have shown that silica pore sizes could be modified by changing the secondary structure of the polyamine [82]. For example, silica composites that are formed by α -helix PLL under basic conditions (pH 11.2) produced 1.5 nm pore sizes, whereas silica formed using PLL β -sheets (heated to $\sim 52^\circ\text{C}$) resulted in larger pore sizes ($\sim 1.5\text{--}8\text{ nm}$). In both cases, silica formation was dependent on the PLL concentration and reaction conditions.

More recently, Tomczak and coworkers have shown that hexagonal silica platelets could be synthesized using PLL as a precursor [83], with the morphology of silica species being tailored according to the molecular weight of the PLL used. Higher molecular-weight PLLs (>100 lysines) produced hexagonal silica platelets, while lower molecular-weight PLLs afforded silica nanospheres. Although PLL is a random coil at near-neutral pH (7.5), electrostatic interactions between the larger PLL templates and the silica promotes an α -helical structure formation during condensation, resulting in hexagonal plates (Figure 1.20).

Gautier and coworkers have also utilized PLL by incorporating the template into the pores of polycarbonate membranes to further control the silica size and morphology [84]. Silica formation within confined spaces is important for a variety of materials applications. For example, silica-encapsulated enzymes integrated into a micro- or nano-filter could be used in catalysis, where the substrate would pass through the membrane, interact with the enzyme, and pass through the filter as the product.

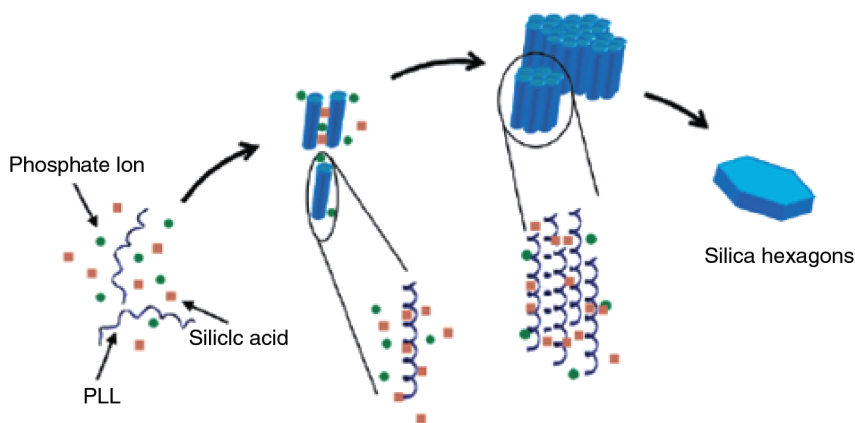


Figure 1.20 Proposed model of PLL-induced condensation of silica platelets. Reprinted with permission from Ref. [83]; © 2005, American Chemical Society.

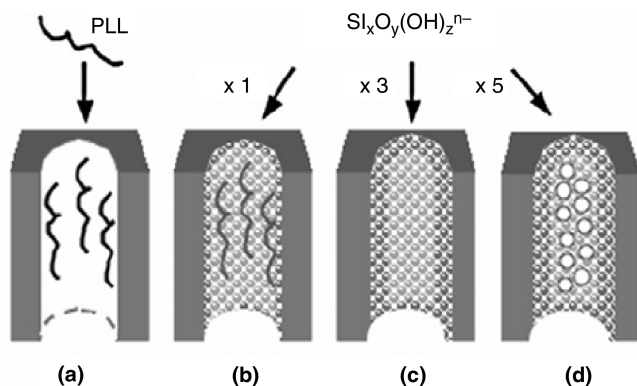


Figure 1.21 Schematic of silica tube formation. (a) PLL is first integrated onto the surface of the pore; (b) Addition of silicates initially results in the formation of a silica shell; (c) Multiple additions of silicates thicken the silica shell; (d) Further addition of silicates results in core particle growth. Reprinted from Ref. [84] with permission from Elsevier.

Rod-like silica tubes were synthesized when PLL was integrated into polycarbonate membrane pores (sizes ranging from 1200, 400 and 200 nm) (Figure 1.21). Multiple successive impregnations (fivefold) of the pores with sodium silicate resulted in the formation of a silica-filled pore, while the thickness of the silica wall decreased as its pore size decreased. In addition, TEM analysis determined that the primary particle diameter was independent of the pore size (~9 nm). However, this primary pore diameter was smaller than for silica formed on the surface (~11 nm), which is most likely the result of PLL localization in the pore rather than of silicate–PLL interactions.

1.5.3.2.4 Polyamines Nonpeptide biomimetic analogues to silica-precipitating peptides are drawn from the isolated LCPAs found on the cell walls of diatoms. Some of these polyamines include poly(allylamine) [79], (PEI) [73], *N*-methylpropylamine (PA) [76] and amine-terminated dendrimers [62, 68–70]. Each of these classes of compound represents a different structural aspect to silica templating, including the number of amines, the number of spacer atoms between the amines, its relative degree of methylation, and the presence and number of branching elements. All of these factors affect the resultant physical properties and subsequent reactivity of the silica nanoparticle produced.

Poly(ethyleneimine) Poly(ethyleneimine) is a branched polyamine ($M_w = 1800$) consisting of a 1:2:1 ratio of primary, secondary and tertiary amines that makes it structurally similar to polyamines isolated from *S. turis* and *C. fusiformis* [85]. These PEIs were integrated as spherical reverse micelles (RMs) made from bis(2-ethylhexyl) sulfosuccinate sodium salt (AOT) in iso-octane, providing a constrained environment for silica precipitation. These RMs exchanged their contents

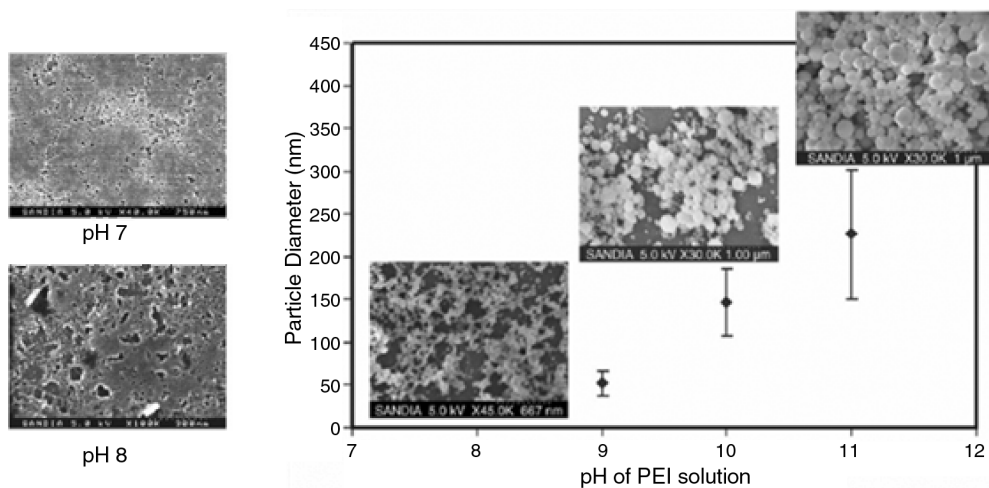


Figure 1.22 Diameter and dispersity of silica particles formed in aqueous PEI solutions at 0.05 M primary-amine concentration and 1 M silicic acid in a 4:1 volume ratio at pH 9, 10 and 11. SEM images of the nanoparticles are provided as inserts, and the silica formed in pH 7 and pH 8 is shown on the left. Reproduced with permission from Ref. [73]; © Wiley-VCH Verlag GmbH & Co. KGaA.

quickly through fusion and redispersion processes ($106\text{--}108\text{ m}^{-1}\text{ s}^{-1}$). Consequently, PEIs reacted with silicic acid from a tetramethylorthosilicate (TMOS) precursor produced silica nanoparticles with a size and structure control that was dependent on the size of the RM [73]. Before testing silica precipitation in the RM, condensation of silica was investigated at a variety of pH values (6.3–11.2) in water. An instantaneous precipitation occurred at basic pH (9–11), a slow deposition of amorphous silica matrix at near-neutral pH, and no precipitation occurred for acidic pH (Figure 1.22).

Consequently, it was expected that PEI would provoke a similar pH dependence when reacted with the RM. However, when PEI and silicic acid were incorporated into the RMs prepared in iso-octane, the initial pH of the amine solution was negligible in terms of controlled silica growth. The pH of the AOT was confirmed with 8-hydroxypyrene-1,3,6-trisulfonic acid (HPTS); it was determined that the local pH remained consistent (≥ 9), independent of the pH of the inserted PEI. In addition, changes in the size of the water pool ($w_0 = 5\text{--}40$, where $w_0 = [\text{H}_2\text{O}]/[\text{AOT}]$) led to the production of a variety of particle sizes. The smallest RMs ($w_0 = 5$) fashioned very small amounts of silica due to the tight interactions between the water molecules, the anionic sulfonate groups of the AOT, and cationic sodium ions. However, larger RMs ($w_0 = 10$) resulted in hollow silica shells with diameters on the order of $1\ \mu\text{m}$. In this case, the RM remained stable during the reaction, and the silica units only interacted by micellar exchange. For the largest RM sizes ($w_0 \geq 20$), destabilization of the RM occurred due to the addition of additional water

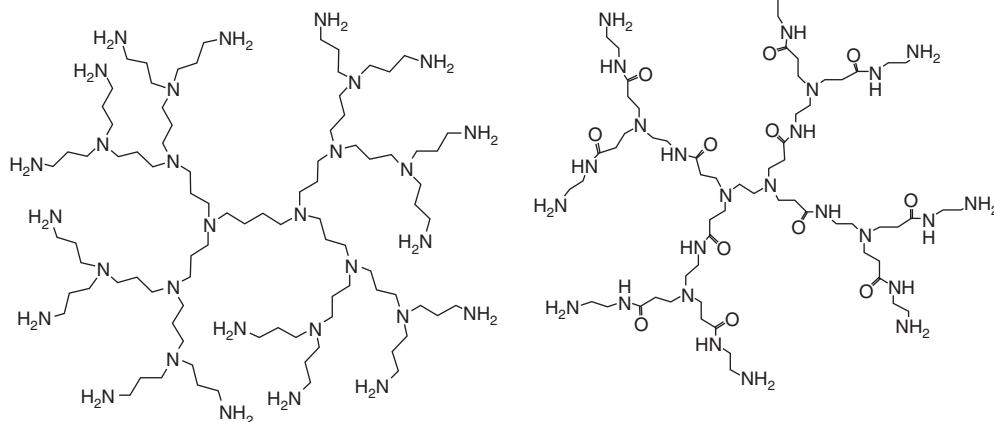


Figure 1.23 Chemical structure of the G-3 PPI dendrimer (left) and G-1 PAMAM dendrimer (right). Reprinted with permission from Ref. [68]; © 2004, American Chemical Society.

molecules in the RM from the condensation of silanol groups, thus increasing the w_0 during the reaction.

Therefore, RMs with an initial $w_0 = 20$ became unstable as soon as the reaction was initiated, and this resulted in tri-modal nanosphere diameter distributions (56 ± 6 , 172 ± 31 and >200 nm, respectively). This suggested multiple destabilization pathways of the RMs during the condensation, resulting in different silica sizes. Moreover, the morphology of the silica was determined by the size of the RM, as well as its stability during the condensation reaction. By understanding the mechanism of this reaction, the sizes and shapes of silica could be tuned to serve a variety of functions, including an inert matrix for catalysis, drug delivery and transport [37].

1.5.3.2.5 Dendrimers Amine-terminated dendrimers are unique, unimolecular polymer templates with defined reactivity as a function generation size (the number of branching elements). Dendrimers have been utilized as a template, capable of localizing a high concentration of biomimetic moieties, including silica [68]. Not only have dendrimers been used as stabilizing templates for sol-gel composites [68], but amine terminated polypropylenimine (PPI) and polyamidoamine (PAMAM) dendrimers have also been used as nonpeptide mimics to the unmodified R5 peptide for the controlled formation of silica nanospheres (Figure 1.23) [62, 68–70].

Positively charged dendrimers only produce silica nanospheres in the presence of an anion, such as phosphate, sulfate or acetate, at pH 7.5. The size of silica produced is dependent on the generation size of the dendrimer, where larger generations produce larger silica nanospheres. Comparisons between the PPI and PAMAM dendrimers have revealed that the PPI dendrimer has a reduced specific

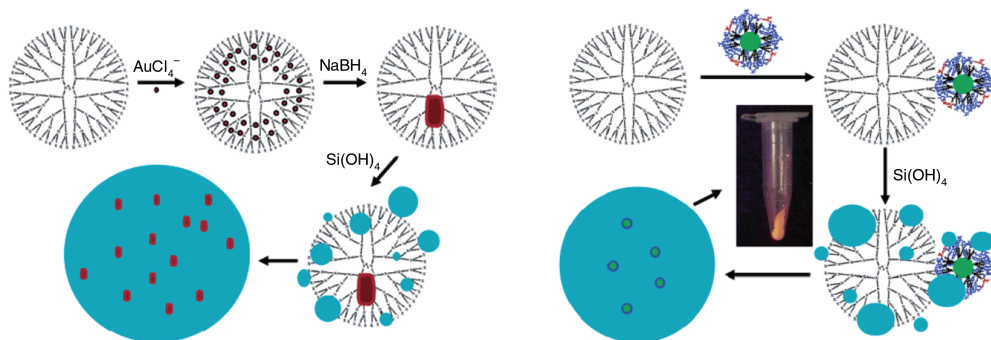


Figure 1.24 Schematic silica encapsulation of Au⁰ nanoparticles (left) and CdSe/ZnS core shell AMP quantum dots. Reprinted with permission from Ref. [69]; © 2004, American Chemical Society.

activity because it precipitates silica much faster than does the PAMAM dendrimer of similar generation size [68]. For this reason, detail of the remaining syntheses will be limited only to the PAMAM dendrimer.

Incorporating known concentrations of dendrimers into the silica matrix has enabled specific morphological control over the nanoparticles under mild conditions. This control could be modified and applied directly to the encapsulation of functional components that are necessary for catalysis, biological labeling and detection, and electronic devices [62, 69]. Generation 4 (G4) PAMAM dendrimers have been used to catalyze the encapsulation of gold nanoparticles and CdSe and ZnS core shell AMP Quantum Dots [69]. In this reaction, cationic gold (Au³⁺) is coordinated to the amine groups of the G4 PAMAM dendrimer, where it is reduced to Au⁰ by NaBH₄. After lyophilization, energy dispersive X-ray spectrometry (EDS) analysis determined that the gold was either surface-passivated or incorporated with within the dendrimer matrix (Figure 1.24).

Although many of the surface dendrimer amines are occluded by the gold or quantum dot nanoparticles, silica condensation still occurs. In fact, the CdSe/ZnS core shell quantum dots with negatively charged surface carboxylates were encapsulated with 99% efficiency, which suggests that the electrostatic attraction between the quantum dots and the templates was sufficient for encapsulation of these materials [69].

Enzymes have also been incorporated into the PAMAM dendrimer to produce silica nanoparticles. At physiological pH, the interaction between an enzyme and the cationic surface of the PAMAM dendrimer plays an important role in forming supramolecular complexes. As a result, the cationic dendrimer (pK_a ~9.5) interacts with low-pI enzymes. For example, glucose oxidase (GO, pI ~4.2) was encapsulated in water with a quantitative yield. As phosphate ions compete with the enzyme, GO was poorly encapsulated as phosphate buffer concentrations increased because the phosphate ions significantly reduced the electrostatic interactions between the enzyme and dendrimer (Figure 1.25).

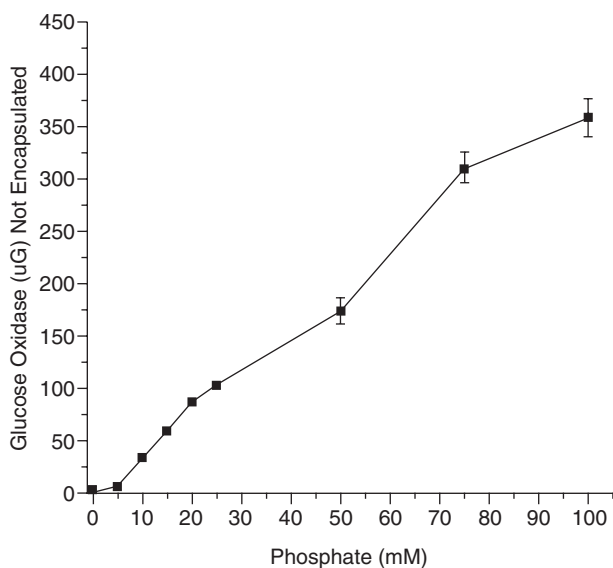


Figure 1.25 Effect of increasing the phosphate buffer concentration on GO encapsulation. Note: initial reactions contained 400 μg of GO. Reproduced with permission from Ref. [62]; © Wiley-VCH Verlag GmbH & Co. KGaA.

A 50% loss in enzymatic activity under optimal conditions was most likely due to unfavorable orientations in the silica framework, or to alterations in steady-state conditions due to a local increase in enzyme concentration in the silica. Long-term storage effects were examined and enzymatic activity was consistent after 30 days of storage at room temperature in buffered solutions. The silica framework provides not only a structural matrix around the enzyme, which physically blocks much of the natural degradation of the enzyme, but also a physical barrier against invading species such as bacteria [62].

1.5.3.2.6 Effects of Variations of Unbranched Polyamines Unbranched polyamines were modified to direct control over the size and morphology of silica composites. In order to assess the role of polyamine structure in controlling the morphology of silica nanoparticles, Belton and coworkers have utilized modified polyamines with different degrees of polymerization, different levels of amine methylation, and different lengths of amine chain spacers (Figure 1.26) [77]. The degree of polymerization was evaluated by comparing two naturally occurring polyamines, spermidine and spermine, to the other synthetic polyamines. Amine methylation was investigated through a set of *N,N'*-(bis-3-aminopropyl)-1,3-diaminopropanes with levels of methylation from 0 to 4. For each experiment, dipotassium tris(1,2-benzenediolato-*O,O'*)silicate served as the silica precursor.

Hollow silica nanoparticles are of particular interest due to their potential applications in adsorptive filters, ultrasound imaging, photonic band gap materials and

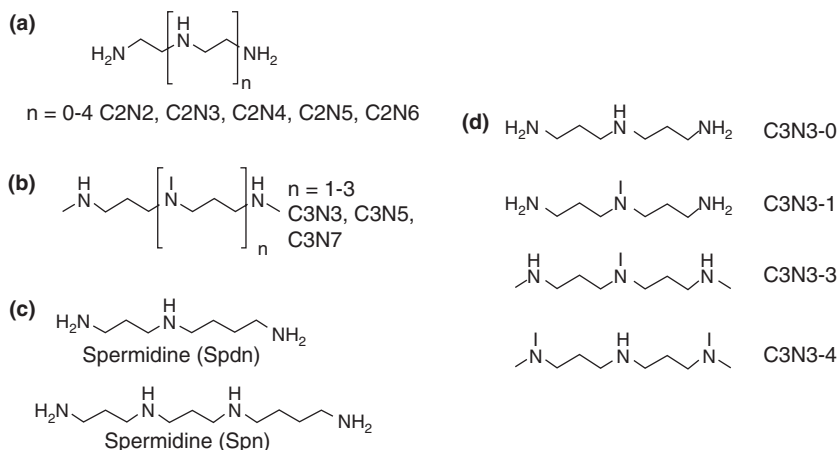


Figure 1.26 Polyamines used in this study. (a) Ethyleneamines; (b) Propylamines; (c) Natural amines spermine and spermidine; (d) C3N3 with varying degrees of methylation. Reproduced with permission from Ref. [77]; © 2008, National Academy of Sciences, USA.

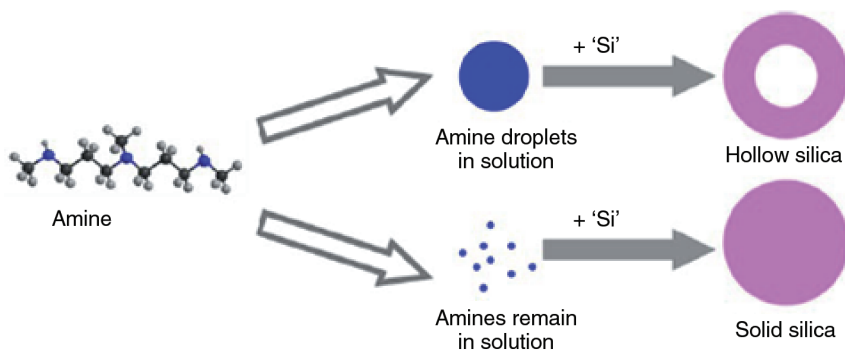


Figure 1.27 Schematic representation of the microemulsion formation leading to hollow silica structures. Reproduced with permission from Ref. [77]; © 2008, National Academy of Sciences, USA.

catalysis [39]. For all of investigated samples, there were mixtures of solid and hollow particles associated with the number of amines per molecule, the amine–amine separation and the size of the polyamine. The larger propylamines, which are the most hydrophobic and most readily form microemulsions, were the most efficient in generating hollow silica nanoparticles.

Two critical factors were identified for controlling the nature of the resultant silica composite in this reaction. First, the template's ability to produce microemulsions determined whether solid or hollow silica was formed (Figure 1.27) [77]. Second, the reaction kinetics of the composite was shown to increase according to the degree of charge associated with the microemulsions. A positively

charged microemulsion introduced a water-free microenvironment, where water removal promoted the condensation of controllable silica.

The kinetics of each silica condensation reaction were quantified using the molybdenum blue method, which is sensitive to monomeric and dimeric silicic acid. Within the initial condensation time, there was a third-order linear relationship between $[\text{Si}(\text{OH})_4]^{2-}$ and time. As a result, it was concluded that polyamines with a threefold increase in their third-order rate constant were kinetically active. C2N2-4 and the naturally occurring polyamines spermidine and spermine observed no rate enhancement. All of the propylamines and longer-chain ethyleneamines significantly influenced condensation rates, with C3N7 having a 14-fold increase in catalytic activity.

Increasing the methylation levels in the C3N3 species also increased the third-order rate constant. For all of the kinetically active species, the silica nanoparticles produced were nonporous, which is most likely due to rapid nucleation. Thus, by modifying the composition of the polyamine, the ability to produce microemulsions which lead to hollow silica and the porosity of the silica can be tailored, leading to the production of a variety of potential nanomaterials [77].

1.5.3.3 Other Biomimetic Templates

Other natural biomimetic templates that utilize amines as the catalytic sites for silica precipitation have also been reported [74, 78]. Cellulose was recently used as a rigid backbone for silica nanotube formation by introducing oligopropylamido side chains derived from dipropylenetriamine (DPTA) to the C-6 position of almost all of the anhydroglucose units (AGUs) (Figure 1.28) [74].

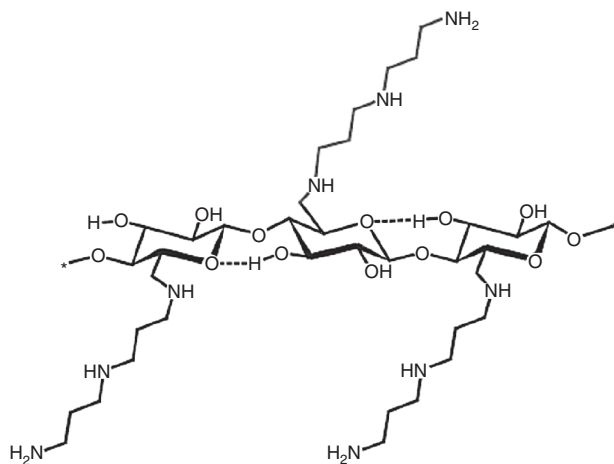


Figure 1.28 Structure of dipropylenetriamine (DPTA) cellulose tosylate. Note that some tosylate residues are present at the C-2 and C-6 positions during the synthesis, as indicated by ^{13}N NMR spectroscopy. Reproduced with permission from Ref. [74]; © 2007, Wiley-VCH Verlag GmbH & Co. KGaA.

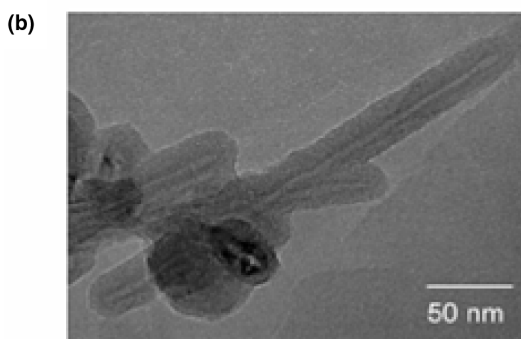
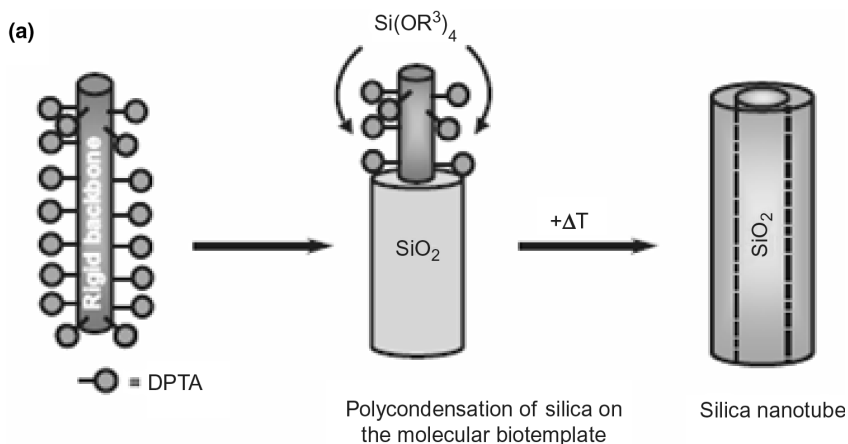


Figure 1.29 (a) Schematic representation of the formation of silica nanotubes from a functionalized biopolymer; (b) TEM images of silica nanotubes formed using the DPTA cellulose tosylate template. Reproduced with permission from Ref. [74]; © 2007, Wiley-VCH Verlag GmbH & Co. KGaA.

These silica nanotubes are technologically significant because they could be used as a nonconductive substitute for carbon nanotubes and as templates for further reactivity. The rigidity of the cellulose backbone exposes its surface amines in water, inducing a hydrogen-bonded amine–silica network (Figure 1.29).

The resultant nanotubes exhibited diameters of 10–30 nm, inner core diameters of ~3 nm, and lengths of up to 500 nm. The proposed mechanism of condensation shows that the silica monomers interact with two amino groups on the DPTA through hydrogen bonding. This localization of silica precursor along the catalytic amine sites of cellulose then induces a lateral growth of nanotubes. Following the initial silica growth, the condensation is repeated (albeit in a disordered fashion), and this results in a tubular coating of amorphous silica [74].

1.5.3.4 Non-natural Metal Oxide Synthesis Using Biomimetic Peptides

Although fewer reports have been made than for the biomimetic synthesis of silica, other metal oxides have also been created under ambient conditions using synthetic and natural templates. For example, germania (GeO_2) was synthesized under ambient conditions and neutral pH with poly (allylamine hydrochloride) (PAH) as the condensation template [86]. The physical and chemical properties of germania are of interest because of its potential application for enhancing optical fibers and other optoelectronic applications [87]. The reaction of PAH and a germanium precursor induced germania nanospheres when the reaction mixture was simply combined, but highly anisotropic rod-like morphologies were observed when the reaction mixture was stirred. This change in morphology was most likely caused by perturbation of the orientation of the self-assembled PAH molecules and solution, which was then followed by nucleation and growth of the germania nanoparticles [86]. These changes in morphology suggest that different types of nanostructures could be formed simply by agitating the reaction mixture at different frequencies.

Titania (TiO_2) has been synthesized incorporating a variety of peptides, including R5 peptide, PLL, spermidine and spermine [88, 89]. Although it is not as naturally abundant as silica, TiO_2 has been identified in the comb of the hornet *Vespa orientalis*, the test (skeleton) of the foraminiferan *Bathysiphon argenteus*, and also in leukocytes and osteosarcomas in humans [89]. Recently, Sewell and coworkers have utilized a PLL and R5 peptide template to catalyze the precipitation of titania nanoparticles (sizes of 80–200 nm and 30–60 nm, respectively) under ambient conditions [88]. Interestingly, the presence of phosphate ions in the R5 peptide reaction had no effect on titania precipitation, unlike that observed for silica. The same was true for the PLL-synthesized titania nanoparticles; in contrast to observations with silica, the length of the PLL chain did not affect the resultant shape of titania nanoparticles. The fact that the latter were all spherical suggested that the titania plays a larger role in its own developing structure than does PLL during condensation [88].

Cole and coworkers have also synthesized titania nanoparticles by incorporating spermidine and spermine as the condensation templates [89]. A SEM analysis of the resultant nanoparticles revealed that the structures were composed of irregular polyhedra, ranging from 100 to 800 nm in diameter for spermidine and from 50 to 300 nm for spermine. A powder analysis showed that both the spermidine- and spermine-templated titania nanoparticles were X-ray amorphous at room temperature. Crystallization was induced at higher temperatures (800 °C). For the spermidine titania, crystalline patterns were evident at 600 °C and 800 °C (Figure 1.30), which corresponded to an anatase phase with trace amounts of rutile.

An interesting pH and temperature dependence of titania formation was also identified. At higher temperatures, the titania nanoparticles for spermidine-templated titania became smaller in diameter, which was predicted to be caused by a faster nucleation rate. Interestingly, there was no notable temperature dependence for the significantly faster spermine-templated titania precipitation over the range of 5–80 °C; at this temperature, the reaction was kinetically faster, negating any temperature effects. A similar trend was observed for pH dependence, where

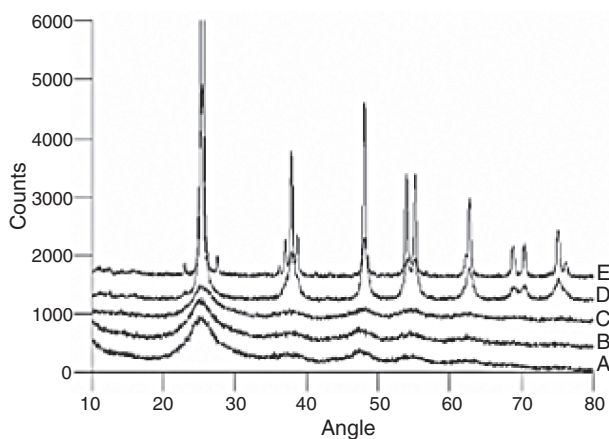


Figure 1.30 X-ray diffraction data from titania precipitated with spermidine and annealed to (A) room temperature, (B) 200°C, (C) 400°C, (D) 600°C and (E) 800°C. Reprinted with permission from Ref. [89]; © 2007, American Chemical Society.

spermine precipitated titania independent of the pH (2.9–12.6). Spermidine-templated precipitation, however, occurred only between pH 5.3–12.6, where polyhydrals were documented in the pH range of 8–9.

1.5.4

Conclusions

Today, as increasing amounts of information are produced relating to the biological mechanisms that drive the silica formation of diatoms, evolved biomimics are being created that will continue to reveal applications beyond catalysis, biosensing and drug delivery. Among all of the templates described here, however, one point is clear—that templates have a major influence on the size and morphology of the silica nanoparticle. For example, the recent discovery of silacidins (polyanions required for silica formation *in vivo*) suggests that the anion might have an effect on the size and morphology of the silica nanoparticles produced. Clearly, a more complete understanding of how factors such as template structure and reaction conditions (i.e. pH, temperature, anion concentration) affect the sizes and shapes of silica nanoparticles will have a profound influence on the investigations of future materials scientists in this area.

1.6

Future Perspectives: Processing Metal Oxide Nanomaterials

Lessons learned from the biomimetic, *in vitro* syntheses of metal oxides have resulted in efficient, low-temperature approaches towards the development of

nanoengineered materials. In fact, these approaches are already being harnessed in the next generation of biomimetic materials, namely 2-D patterned metal oxides. For example, a number of different deposition techniques for biomimetic patterning have been incorporated to mimic the microstructure of the diatom cell wall. Specifically, techniques which include solenoid jet printing, lithographic patterning and direct ink writing (DIW) have been used to deposit a variety of silica-precipitating precursors [90–92]. Coffman and coworkers have used both solenoid jet printing and photolithography to pattern PLL and (3-aminopropyl)-trimethoxysilane, respectively. Although these methods have provided a unique approach towards developing a controllable template for silica precipitation, they have been limited either by large, non-uniform spots (solenoid jet printing), or by smaller, unresolved spots (lithography) [90].

Rapid prototyping techniques using computer-aided deposition have been developed to eradicate these setbacks. For instance, Xu and coworkers have integrated DIW to directly deposit ($40\ \mu\text{m s}^{-1}$) polyamine-rich inks [91]. In these experiments, polyelectrolyte inks were loaded into a syringe and robo-casted onto a substrate using a computer-animated design. The patterned surfaces were then hydrolyzed with silicic acid to condense the micropatterned silica. When auger electron microscopy was used to map the distribution of silica along the patterns, both silicon and oxygen were seen to be distributed uniformly about the pattern [91].

Using a different approach, Kisailus and coworkers integrated soft-lithography stamping to micropattern $\gamma\text{-Ga}_2\text{O}_3$ using a selection of catalytic enzymes associated with silicatein peptides [92]. Here, thiolated ligands composed of nucleophilic hydroxyl and hydrogen-bonded amine moieties derived from silicatein were assembled onto poly(dimethylsiloxane) (PDMS) stamps which were then applied to gold substrates and reacted with precursor solution. The strong binding affinity between the $-\text{SH}$ group and gold substrates induced the formation of hydroxyl self-assembled monolayers (SAMs) available for further reactivity [92]. In fact, once immersed in a precursor solution of gallium nitrate, these hydroxyl groups served as a site for the condensation of $\gamma\text{-Ga}_2\text{O}_3$. The surface energy of the ordered monolayers provided a defined area for hydrolysis of gallium nitrate and subsequent ripening, dissolution and precipitation of $\gamma\text{-Ga}_2\text{O}_3$. This control could be used for the surface-catalyzed systems at low temperatures for novel electronic or optical applications.

Additional rapid prototyping techniques today are beginning to attract interest in biomaterials deposition. One such technique—piezoelectric inkjet printing—is a noncontact method that employs a user-controlled waveform to deposit known amounts of material onto a variety of substrates [93]. With the advent of such readily available deposition techniques, even more metal oxides could be printed on the 2-D scale [88, 93]. The constrained and unconstrained syntheses of metal oxides reported to date can now be incorporated with these newer technologies to bridge the *in vitro* and macromolecular worlds of biology and materials science, together expanding new frontiers in nanomaterial design.

References

- 1 Wolf, S. (2004) *Microchip Manufacturing*, Lattice Press, Sunset Beach.
- 2 Kumar, U., Shete, A., Harle, A.S., Kasyutich, O., Schwarzacher, W., Pundle, A. and Poddar, P. (2008) Extracellular bacterial synthesis of protein functionalized ferromagnetic Co₃O₄ nanocrystals and imaging of self-organization of bacterial cells under stress after exposure to metal ions. *Chemistry of Materials*, **20**, 1484–91.
- 3 Weiner, S. and Dove, P.M. (2003) *An Overview of Biomineralization Processes and the Problem of the Vital Effect*, Vol. 54, The Mineralogical Society of America, Washington, DC.
- 4 Bar-Cohen, Y. (2006) Biomimetics—using nature to inspire human innovation. *Bioinspired Biomimicry*, **1**, 1–12.
- 5 Carney, C.K., Harry, S.R. and Sewell, S.L. (2007) Detoxification biominerals. *Topics in Current Chemistry*, **270**, 155–85.
- 6 Gorna, K., Munoz-Espi, R., Grohn, F. and Wegner, G. (2007) Bioinspired mineralization of inorganics from aqueous media controlled by synthetic polymers. *Macromolecular Biosciences*, **7**, 163–73.
- 7 Perry, C.C. (1998) *Biomaterials*, John Wiley & Sons, Inc., New York.
- 8 Fratzl, P. (2007) Biomimetic materials research: what can we really learn from nature's structural materials? *Journal of the Royal Society Interface*, **4**, 637–42.
- 9 Douglas, T. and Young, M. (2006) Viruses: making friends with old foes. *Science*, **312**, 873–5.
- 10 Douglas, T. and Young, M. (1999) Virus particles as templates for materials synthesis. *Advanced Materials*, **11**, 679–81.
- 11 Lakshminarayanan, R., Vivekanandan, S., Samy, R.P., Banerjee, Y., Chi-Jin, E.O., Teo, K.W., Jois, S.D.S., Kini, M. and Valiyaveettil, S. (2008) Structure, self-assembly, and dual role of a b-defensin-like peptide from the Chinese soft-shell turtle eggshell matrix. *Journal of the American Chemical Society*, **130**, 4660–8.
- 12 Lee, H., Dellatore, S.M., Miller, W.M. and Messersmith, P.B. (2007) Mussel-inspired surface chemistry for multifunctional coatings. *Science*, **318**, 426–30.
- 13 Kroger, N., Deutzmann, R. and Sumper, M. (1999) Polycationic peptides from diatom biosilica that direct silica nanosphere formation. *Science*, **286**, 1129–32.
- 14 Sumper, M. (2002) A phase separation for the nanopatterning of diatom biosilica. *Science*, **295**, 2430–3.
- 15 Zurcher, S., Wackerlin, D., Bethuel, Y., Malisova, B., Textor, M., Tosatti, S. and Gademann, K. (2006) Biomimetic surface modifications based on the cyanobacterial iron chelator anachelin. *Journal of the American Chemical Society*, **128**, 1064–5.
- 16 Henrich, V.E. and Cox, P.A. (1994) *The Surface Science of Metal Oxides*, Cambridge University Press, Boston.
- 17 Lang, C., Schuler, D. and Faivre, D. (2007) Synthesis of manetite nanoparticles for bio- and nanotechnology: genetic engineering and biomimetics of bacterial magnetosomes. *Macromolecular Biosciences*, **7**, 144–51.
- 18 Jun, Y.-W., Seo, J.-W. and Cheon, J. (2008) Nanoscaling laws of magnetic nanoparticles and their applicabilities in biomedical sciences. *Accounts of Chemical Research*, **41**, 170–89.
- 19 Whaley, S.R., English, D.S., Hu, E.L., Barbara, P.F. and Belcher, A.M. (2000) Selection of peptides with semiconductor binding specificity for directed nanocrystal assembly. *Nature*, **405**, 665–8.
- 20 Lippard, S.J. and Berg, J.M. (1994) *Principles of Bioinorganic Chemistry*, University Science Books, Mill Valley.
- 21 Nakanishi, H. and Kahn, M. (1998) *Peptide Mimetics*, Oxford University Press, New York.
- 22 Brown, S. (1997) Metal-recognition by repeating polypeptides. *Nature Biotechnology*, **15**, 269–72.
- 23 Chen, W. and Georgiou, G. (2002) Cell-surface display of heterologous proteins: from high-throughput screening to environmental applications. *Biotechnology and Bioengineering*, **79**, 496–503.

- 24 Wittrup, K.D. (2001) Protein engineering by cell-surface display. *Current Opinion in Biotechnology*, **12**, 395–9.
- 25 Tomczak, M.M., Slocik, J.M., Stone, M.O. and Naik, R.R. (2007) Bio-inspired approaches to inorganic material synthesis. *Biochemical Society Transactions*, **35**, 512–15.
- 26 Poole, C.P. and Owens, F.J. (2003) *Introduction to Nanotechnology*, John Wiley & Sons, Inc., Hoboken.
- 27 Liu, W.-T. (2006) Nanoparticles and their biological applications. *Journal of Bioscience and Bioengineering*, **102**, 1–7.
- 28 Klem, M.T., Resnick, D.A., Gilmore, K., Young, M., Idzerda, Y.U. and Douglas, T. (2007) Synthetic control over magnetic moment and exchange bias in all-oxide materials encapsulated within a spherical protein cage. *Journal of the American Chemical Society*, **129**, 197–201.
- 29 Oaki, Y. and Imai, H. (2005) The hierarchical architecture of naacre and its mimetic material. *Angewandte Chemie*, **117**, 6729–33.
- 30 Yahiro, J., Oaki, Y. and Imai, H. (2006) Biomimetic synthesis of wurzite ZnO nanowires possessing a mosaic structure. *Small*, **2**, 1183–7.
- 31 Oaki, Y. and Imai, H. (2006) Nanoengineering in echinoderms: the emergence of morphology from nanobricks. *Small*, **2**, 66–70.
- 32 Bansal, V., Poddar, P., Ahmad, A. and Sastry, M. (2006) Room-temperature biosynthesis of ferroelectric barium titanate nanoparticles. *Journal of the American Chemical Society*, **128**, 11958–63.
- 33 Herrera-Becerra, R., Zorrilla, C. and Ascencio, J.A. (2007) Production of iron oxide nanoparticles by a biosynthesis method: an environmentally friendly route. *Journal of Physical Chemistry C*, **111**, 16147–53.
- 34 Theil, E.C., Sayers, D.E. and Brown, M. A. (1970) Similarity of the structure of ferritin and iron dextran (imferon) determined by extended X-ray absorption fine structure analysis. *Journal of Biological Chemistry*, **17**, 8132–4.
- 35 Klem, M.T., Mosolf, J., Young, M. and Douglas, T. (2008) Photochemical mineralization of europium, titanium, and iron oxyhydroxide nanoparticles in the ferritin protein cage. *Inorganic Chemistry*, **47**, 2237–9.
- 36 Uchida, M., Klem, M.T., Allen, M., Suci, P., Flenniken, M., Gillitzer, E., Varpness, Z., Liepold, L.O., Young, M. and Douglas, T. (2007) Biological containers: protein cages as multifunctional nanoplatfoms. *Advanced Materials*, **19**, 1025–42.
- 37 Loste, E., Park, R.J., Warren, J. and Meldrum, F.C. (2004) Precipitation of calcium carbonate in confinement. *Advanced Functional Materials*, **14**, 1211–20.
- 38 Lee, S.-Y., Gao, X. and Matsui, H. (2007) Biomimetic and aggregation-driven crystallization route for room-temperature material synthesis: growth of beta-Ga₂O₃ nanoparticles on peptide assemblies as nanoreactors. *Journal of the American Chemical Society*, **129**, 2954–8.
- 39 Nuraje, N., Su, K., Haboosheh, A., Samson, J., Manning, E.P., Yang, N.-I. and Matsui, H. (2006) Room temperature synthesis of ferroelectric barium titanate nanoparticles using peptide nanorings as templates. *Advanced Materials*, **18**, 807–11.
- 40 Zhang, W., Zhang, D., Fan, T., Ding, J., Guo, Q. and Ogawa, H. (2006) Fabrication of ZnO microtubes with adjustable nanopores on the walls by the templating of butterfly wing scales. *Nanotechnology*, **17**, 840–4.
- 41 Biro, L.P., Balint, Z., Kertesz, K., Vertesy, Z., Mark, G.I., Tapasztó, L., Vigneron, J.-P., Lousse, V. and Biro, L.P. (2007) Photonic crystal structures of biologic origin: butterfly wing scales. *Materials Research Society Symposium Proceedings*, **1014**, AA07-08-16.
- 42 Zhang, W., Zhang, D., Fan, T., Ding, J., Gu, J., Guo, Q. and Ogawa, H. (2006) Biomimetic zinc oxide replica with structural color using butterfly (*Ideopsis similis*) wings as templates. *Bioinspired Biomimcry*, **1**, 89–95.
- 43 Zou, D., Xu, C., Luo, H., Wang, L. and Ying, T. (2008) Synthesis of Co₃O₄ nanoparticles via an ionic liquid-assisted methodology at room temperature. *Materials Letters*, **62**, 1976–8.

- 44 Wilkes, J.S. and Zaworotko, M.J. (1992) *Chemical Communications*, **13**, 965–7.
- 45 Kröger, N. (2007) Prescribing diatom morphology: toward genetic engineering of biological nanomaterials. *Current Opinion in Chemical Biology*, **11**, 662–9.
- 46 Aizenberg, J., Hanson, J., Koetzle, T.F., Weiner, S. and Addadi, L. (1997) *Journal of the American Chemical Society*, **119**, 881–6.
- 47 Oaki, Y. and Imai, H. (2007) Biomimetic morphological design for manganese oxide and cobalt hydroxide nanoflakes with a mosaic interior. *Journal of Materials Chemistry*, **17**, 316–21.
- 48 Vazquez-Olmos, A., Redon, R., Rodriguez-Gattorno, G., Mata-Zamora, M.E., Morales-Leal, F., Fernandez-Osrio, A.L. and Saniger, J.M. (2005) *Journal of Colloid and Interface Science*, **291**, 175.
- 49 Gröger, C., Lutz, K. and Brunner, E. (2008) Biomolecular self-assembly and its relevance in silica biomineralization. *Cell Biochemistry and Biophysics*, **50**, 23–39.
- 50 Sumper, M. (2002) A phase separation model for the nanopatterning of diatom biosilica. *Science*, **295**, 2430–3.
- 51 Halas, N.J. (2008) Nanoscience under glass: the versatile chemistry of silica nanostructures. *ACS Nano*, **2**, 179–83.
- 52 Noll, F., Sumper, M. and Hampp, N. (2002) Nanostructure of diatom silica surfaces and of biomimetic analogues. *Nano Letters*, **2**, 91–5.
- 53 Brunner, E. and Lutz, K. (eds) (2007) *Handbook of Biomineralization: Biomimetic and Bioinspired Chemistry*, Vol. 2, Wiley-VCH Verlag GmbH, Weinheim.
- 54 Christiansen, S.C., Hedin, N., Epping, J.D., Janicke, M.T., del Amo, Y., Demarest, M., Brzezinski, M. and Chmelka, B.F. (2006) Sensitivity considerations in polarization transfer and filtering using dipole-dipole couplings: implications for biomineral systems. *Solid State Nuclear Magnetic Resonance*, **29**, 170–82.
- 55 Sumper, M. and Brunner, E. (2006) Learning from diatoms: nature's tools for the production of nanostructured silica. *Advanced Functional Materials*, **16**, 17–26.
- 56 Poulsen, N. and Kroger, N. (2004) Silica morphogenesis by alternative processing of silaffins in the diatom *Thalassiosira pseudonana*. *Journal of Biological Chemistry*, **279**, 42993–9.
- 57 Poulsen, N., Sumper, M. and Kroger, N. (2003) Biosilica formation in diatoms: characterization of native silaffin-2 and its role in silica morphogenesis. *Proceedings of the National Academy of Sciences of the United States of America*, **100**, 12075–80.
- 58 Wenzl, S., Hett, R., Richthammer, P. and Sumper, M. (2008) Silacidins: highly acidic phosphopeptides from diatom shells assist in silica precipitation in vitro. *Angewandte Chemie International Edition*, **47**, 1729–32.
- 59 Kroger, N., Deutzmann, R., Bergsdorf, C. and Sumper, M. (2000) Species-specific polyamines from diatoms control silica morphology. *Proceedings of the National Academy of Sciences of the United States of America*, **97**, 14133–8.
- 60 Sumper, M. and Kroger, N. (2004) Silica formation in diatoms: the function of long-chain polyamines and silaffins. *Journal of Materials Chemistry*, **14**, 2059–65.
- 61 Naik, R.R., Tomczak, M.M., Luckarift, H.R., Spain, J.C. and Stone, M.O. (2004) Entrapment of enzymes and nanoparticles using biomimetically synthesized silica. *Chemical Communications*, 1684–5.
- 62 Miller, S.A., Hong, E.D. and Wright, D. (2006) Rapid and efficient enzyme encapsulation in a dendrimer silica nanocomposite. *Macromolecular Bioscience*, **6**, 839–45.
- 63 Pouget, E., Dujardin, E., Cavalier, A., Moreac, A., Valery, C., Marchi-Artzner, V., Weiss, T., Renault, A., Paternostre, M. and Artzner, F. (2007) Hierarchical architectures by synergy between dynamical template self-assembly and biomineralization. *Nature Materials*, **6**, 434–9.
- 64 Wong Po Foo, C., Patwardhan, S.V., Belton, D.J., Kitchel, B., Anastasiades, D., Huang, J., Naik, R.R., Perry, C.C. and Kaplan, D.L. (2006) Novel nanocomposites from spider silk-silica fusion (chimeric) proteins. *Proceedings of the National Academy of Sciences of the United States of America*, **103**, 9428–33.

- 65 Zhang, Y., Wu, H., Li, J., Li, L., Jiang, Y., Jiang, Y. and Jiang, Z. (2008) Protamine-templated biomimetic hybrid capsules: efficient and stable carrier for enzyme encapsulation. *Chemistry of Materials*, **20**, 1041–8.
- 66 Luckarift, H.R., Spain, J.C., Naik, R.R. and Stone, M.O. (2004) Enzyme immobilization in a biomimetic silica support. *Nature Biotechnology*, **22**, 211–13.
- 67 Marner, W.D., Shaikh, A.S., Muller, S.J. and Keasling, J.D. (2008) Morphology of artificial silica matrices formed via autossilification of a silaffin/protein polymer chimera. *Biomacromolecules*, **9**, 1–5.
- 68 Knecht, M.R. and Wright, D.W. (2004) Amine-terminated dendrimers as biomimetic templates for silica nanosphere formation. *Langmuir*, **20**, 4728–32.
- 69 Knecht, M.R. and Wright, D.W. (2004) Dendrimer-mediated formation of multicomponent nanospheres. *Chemistry of Materials*, **16**, 4890–5.
- 70 Knecht, M.R., Sewell, S.L. and Wright, D.W. (2005) Size control of dendrimer-templated silica. *Langmuir*, **21**, 2058–61.
- 71 Jan, J.S., Lee, S., Carr, C.S. and Shantz, D.F. (2005) Biomimetic synthesis of inorganic nanospheres. *Chemistry of Materials*, **17**, 4310–17.
- 72 Jan, J.-S. and Shantz, D.F. (2007) Biomimetic silica formation: effect of block copolypeptide chemistry and solution conditions on silica nanostructure. *Advanced Materials*, **19**, 2951–6.
- 73 Bauer, C.A., Robinson, D.B. and Simmons, B.A. (2007) Silica particle formation in confined environments via bioinspired polyamine catalysis at near-neutral pH. *Small*, **3**, 58–62.
- 74 Zollfrank, C., Scheel, H. and Greil, P. (2007) Regioselectively ordered silica nanotubes by molecular templating. *Advanced Materials*, **19**, 984–7.
- 75 Cha, J.N., Stucky, G.D., Morse, D.E. and Deming, T.J. (2000) Biomimetic synthesis of ordered silica structures mediated by block copolypeptides. *Nature*, **403**, 289–92.
- 76 Annenkov, V.V., Patwardhan, S.V., Belton, D., Danilovtseva, E.N. and Perry, C.C. (2006) A new stepwise synthesis of a family of propylamines derived from diatom silaffins and their activity in silicification. *Chemical Communications*, 1521–3.
- 77 Belton, D.J., Patwardhan, S.V., Annenkov, V.V., Danilovtseva, E.N. and Perry, C.C. (2008) From biosilicification to tailored materials: optimizing hydrophobic domains and resistance to protonation of polyamines. *Proceedings of the National Academy of Sciences of the United States of America*, **105**, 5963–8.
- 78 Chang, J.S., Kong, Z.L., Hwang, D.F. and Chang, K.L.B. (2006) Chitosan-catalyzed aggregation during the biomimetic synthesis of silica nanoparticles. *Chemistry of Materials*, **18**, 702–7.
- 79 Lutz, K., Groger, C., Sumper, M. and Brunner, E. (2005) Biomimetic silica formation: analysis of the phosphate-induced self-assembly of polyamines. *Physical Chemistry Chemical Physics*, **7**, 2812–15.
- 80 Wong, M.S., Cha, J.N., Choi, K.S., Deming, T.J. and Stucky, G.D. (2002) Assembly of nanoparticles into hollow spheres using block copolypeptides. *Nano Letters*, **2**, 583–7.
- 81 Brunner, E. (2007) Biomimetic synthesis: double-walled silica nanotubes. *Nature Materials*, **6**, 398–9.
- 82 Hawkins, K.M., Wang, S.S.S., Ford, D.M. and Shantz, D.F. (2004) Poly-L-lysine templated silicas: using polypeptide secondary structure to control oxide pore architectures. *Journal of the American Chemical Society*, **126**, 9112–19.
- 83 Tomczak, M.M., Glawe, D.D., Drummy, L.F., Lawrence, C.G., Stone, M.O., Perry, C.C., Pochan, D.J., Deming, T.J. and Naik, R.R. (2005) Polypeptide-templated synthesis of hexagonal silica platelets. *Journal of the American Chemical Society*, **127**, 12577–82.
- 84 Gautier, C., Lopez, P.J., Livage, J. and Coradin, T. (2007) Influence of poly-L-lysine on the biomimetic growth of silica tubes in confined media.

- Journal of Colloid and Interface Science*, **309**, 44–8.
- 85** Sumper, M. Lorenz, S. and Brunner, E. (2003) Biomimetic control of size in the polyamine-directed formation of silica nanospheres. *Angewandte Chemie International Edition*, **42**, 5192–5.
- 86** Patwardhan, S.V. and Clarkson, S.J. (2005) Bioinspired mineralisation: macromolecule mediated synthesis of amorphous germania structures. *Polymer*, **46**, 4474–9.
- 87** Margaryan, A.A. and Liu, W. (1993) Prospects of using germanium-dioxide-based glasses for optics. *Optical Engineering*, **32**, 1995–6.
- 88** Sumerel, J., Lewis, J., Doraiswamy, A., Deravi, L.F., Sewell, S.L., Gerdon, A.E., Wright, D.W. and Narayan, R.J. (2006) Piezoelectric ink jet processing of materials for medical and biological applications. *Biotechnology Journal*, **1**, 976–87.
- 89** Cole, K.E. and Valentine, A.M. (2007) Spermidine and spermine catalyze the formation of nanostructured titanium oxide. *Biomacromolecules*, **8**, 1641–7.
- 90** Coffman, E.A., Melechko, A.V., Allison, D.P., Simpson, M.L. and Doktycz, M.J. (2004) Surface patterning of silica nanostructures using bio-inspired templates and directed synthesis. *Langmuir*, **20**, 8431–6.
- 91** Xu, M., Gratson, G.M., Duoss, E.B., Shepherd, R.F. and Lewis, J.A. (2006) Biomimetic silicification of 3D polyamine-rich scaffolds assembled by direct ink writing. *Soft Matter*, **2**, 205.
- 92** Kisailus, D., Truong, Q., Amemiya, Y., Weaver, J.C. and Morse, D.E. (2006) Self-assembled bifunctional surface mimics an enzymatic and templating protein for synthesis of a metal oxide semiconductor. *Proceedings of the National Academy of Sciences of the United States of America*, **103**, 5652–7.
- 93** Deravi, L.F., Sumerel, J.L., Gerdon, A.E., Cliffel, D.E. and Wright, D.W. (2007) Output analysis of materials inkjet printer. *Applied Physics Letters*, **91**, 113114–16.